ADVANCING EARTH AND SPACE SCIENCES

JGR Planets

RESEARCH ARTICLE

10.1029/2025JE008987

Special Collection:
Dust-related processes on Mars: Observations, Simulations, and Experiments

Key Points:

- We developed a new method to retrieve atmospheric dust optical depth on Mars using the opaque CO_2 band at 2.77 μm
- 146 local dust storm events were detected. Statistics analysis shows peak frequencies around noon, suggesting initiation in the morning
- Local dust storm spatial patterns vary seasonally, which could be influenced by atmospheric circulation

Correspondence to:

A. Kazama,
kazama.akira.s2@dc.tohoku.ac.jp

Citation:

Kazama, A., Aoki, S., Leseigneur, Y., Vincendon, M., Kasaba, Y., Nakagawa, H., et al. (2025). A statistical study of local dust storm occurrences on Mars using the 2.77 μm CO_2 band observed by OMEGA/ Mars express. *Journal of Geophysical Research: Planets*, *130*, e2025JE008987. https://doi.org/10.1029/2025JE008987

Received 6 FEB 2025
Accepted 25 AUG 2025

A Statistical Study of Local Dust Storm Occurrences on Mars Using the 2.77 μm CO_2 Band Observed by OMEGA/ Mars Express

Akira Kazama[1,2], Shohei Aoki[2,3], Yann Leseigneur[4], Mathieu Vincendon[5], Yasumasa Kasaba[1], Hiromu Nakagawa[1], Thomas Gautier[4,6], Aymeric Spiga[7], Tanguy Bertrand[6,8], Franck Montmessin[4], Kazunori Ogohara[9], Takeshi Imamura[2], Isao Murata[1], and John Carter[5,10]

[1]Graduate School of Science, Tohoku University, Sendai, Japan, [2]Graduate School of Frontier Sciences, University of Tokyo, Kashiwa, Japan, [3]Royal Belgian Institute for Space Aeronomy, Brussels, Belgium, [4]LATMOS/IPSL, UVSQ Université Paris-Saclay, Sorbonne Université, CNRS, Guyancourt, France, [5]Institut d'Astrophysique Spatiale, Université Paris-Saclay, CNRS, Orsay, France, [6]LIRA, Observatoire de Paris, Université PSL, Sorbonne Université, Université Paris Cité, CY Cergy Paris Université, CNRS, Meudon, France, [7]Sorbonne Université, Laboratoire de Météorologie Dynamique (LMD/IPSL), Paris, France, [8]LPGN, CNRS, UMR6112, Université Nantes, Nantes, France, [9]Faculty of Science, Kyoto Sangyo University, Kyoto, Japan, [10]LAM, Aix-Marseille Université, CNRS, Marseille, France

Abstract Local Dust Storms (LDS) are defined as dust storm phenomena that cover an area smaller than 1.6×10^6 km^2 or persist for less than three sols. The study of LDS is critical for understanding dust transport processes in both horizontal and vertical directions and the evolution of large-scale dust storms on Mars. However, the relatively small scale and short lifetime make it difficult to detect with previous studies. OMEGA onboard Mars Express (MEx) has conducted spectroscopic measurements with high spatial resolution (up to ∼400 m/pixel). Here, we present a method to retrieve dust optical depth and detect LDS using the 2.77 μm CO_2 absorption band. At this wavelength, photons are absorbed before reaching the surface, and the photons collected by OMEGA have been scattered around 20–30 km altitude by dust. We have detected 146 LDS events from the retrieved dust optical depth in MY27-29. The LDS were generally observed in the southern summer season, while frequent occurrences of LDS were observed during the northern summer (Ls = 130°–150°) in MY27. The remarkable increase in LDS is also identified just before the global dust storm in MY28. We found a peak in the probability of LDS around noon in both seasons, Ls = 0°–180° and Ls = 180°–360°. In Ls = 0°–180°, high probability areas are found only in specific regions, such as Chryse Planitia. The probability areas expands over a wide range, except high-latitude north of 40°N in Ls = 180°–360°. These findings highlight the spatiotemporal roles LDS play in dust transport, providing insights into the dust cycle (245/250 words).

Plain Language Summary Dust storms are important for Martian meteorology because they move dust from the surface into the atmosphere. This study focuses on small dust storms, called LDS, which may play a role in developing larger storms. We used infrared data from the OMEGA, a spectrometer onboard the European spacecraft Mars Express. Using these data, we developed a method to detect dust at 20–30 km above the surface using the radiance observed at 2.77 μm. We applied this method to data from 2004 to 2011 (corresponding to Mars Years 27–29) and identified 146 LDS events. These storms occurred most often during the southern summer on Mars. However, an unusual increase in LDS was seen during the northern summer in 2004–2006. We also found that most storms occurred around midday, suggesting that they begin to form in the morning. The locations of storms changed with the seasons: during northern summer, storms were concentrated in a single area, whereas during southern summer, they occurred in many regions, except for the high northern latitudes (above 40°N). Our method could be applied to data from other Mars missions and may help improve our understanding of how dust moves through the Martian atmosphere.

1. Introduction

Dust is a key parameter of the Martian atmosphere, controlling its heating through direct absorption of solar radiation. Atmospheric heating drives the heat engine of the entire atmosphere, impacting its structure and dynamics. The latter dictates in return the amplitude of fluctuations in dust, leading to a feedback loop responsible for various meteorological phenomena that are observed on Mars and that occur at different scales. These meteorological phenomena exhibit longer timescales as their spatial scale increases (e.g., Sánchez-Lavega et al., 2024, Figure 1). Moreover, it is well established that seasonal changes in the distance between the Sun and Mars are responsible for the strong seasonal variability of dust in the atmosphere. Typically, dust activity in the atmosphere is weaker near the aphelion (solar longitude (Ls) = 0°–180°) and increases toward the perihelion (Ls = 180°–360°) (e.g., Montabone et al., 2015; Smith & Smith, 2004).

Dust storms on Mars are generally classified into three categories: local-scale, regional-scale, and global-scale. This classification is based on storm area and duration, with local dust storms (LDS) covering less than 1.6×10^6 km^2 or having a duration of <3 sols (Martian days), regional dust storms (RDS) extending over more than 1.6×10^6 km^2 and persisting for more than three sols (Cantor et al., 2001), and global dust storms (GDS) encircling the planet over most of the latitudes with a duration of tens to hundreds of sols. Previous studies on RDS have mainly used visible and ultraviolet imaging observations from orbiters to statistically investigate their spatiotemporal behavior (Battalio & Wang, 2021; Wang & Richardson, 2015). Regional dust storms primarily occur during the Ls = 180°–360°, coinciding with increased atmospheric dust, and can be categorized by periods such as the A-storm period (around Ls = 210°–240°), the B-storm period (around Ls = 250°–270°), and the C-storm period (around Ls = 300°–310°) (Kass et al., 2016). While the development mechanisms of these RDS remain partially unexplored or unknown, there is evidence that LDS merge to form RDS (Cantor et al., 2001; Hinson & Wang, 2010; Martin & Zurek, 1993; Wang & Richardson, 2015). In addition, LDS, such as rocket dust storms (Määttänen et al., 2009; Spiga et al., 2013), play a significant role in transporting dust both horizontally and vertically. Understanding LDS behavior is thus critical to elucidate the mechanisms underlying larger-scale RDS dust storm development. However, LDS are challenging to observe due to their small spatial and temporal scales.

Previous observations from visible and ultraviolet imaging have provided detailed insights into the scale, location, and seasonal variations of dust storms on Mars (e.g., Battalio & Wang, 2021; Leseigneur & Vincendon, 2023; Montabone et al., 2015; Smith et al., 2001). More recently, Guha et al. (2024) used the Emirates Exploration Imager aboard the Emirates Mars Mission (EMM) to systematically study the temporal and seasonal behavior of regional/LDS based on visible and UV imaging data. While these observations can be used to estimate dust optical depth (Cantor et al., 2001), infrared spectroscopic observations are essential for in-depth quantitative assessment of dust concentration, which is an important parameter for understanding the formation process of dust storms. The behavior of global dust concentration on Mars has been studied using infrared instruments such as the Thermal Emission Spectrometer aboard Mars Global Surveyor, the Thermal Emission Imaging System aboard Mars Odyssey, and, more recently, the Emirates Mars InfraRed Spectrometer (EMIRS) aboard the EMM (e.g., Montabone et al., 2015; Smith et al., 2001; Smith et al., 2022). However, these instruments have limitations in spatial resolution or local time coverage, which make it challenging to characterize the local-scale and diurnal variability of LDS. While recent instruments such as EMIRS provide observations at varying local times, their coarse spatial resolution limits their ability to resolve small-scale dust storm activity. As a result, there are relatively few statistical studies using infrared data sets that quantitatively resolve small-scale events. More detailed investigations using higher-resolution infrared data sets are therefore essential for improving our understanding of small-scale dust dynamics and enhancing the reliability of dust parameterizations in numerical models (e.g., Wang et al., 2018).

A near-infrared imaging spectrometer, Observatoire pour la Minéralogie, l'Eau, les Glaces et l'Activité (OMEGA) onboard Mars Express (MEx), can observe atmospheric variations on Mars with high spatial resolution. Because of the precession of the orbit plan, observations can be conducted at different local times. This feature is expected to capture the spatial-temporal and local time variability of dust optical depth at smaller scales, which has been lacking in previous studies. Several studies have reported on retrieving dust optical depth using OMEGA data. Some methods were developed specifically for the polar regions of Mars (Vincendon et al. (2007, 2008); Douté et al. (2013); Douté (2013)). At lower latitudes, Vincendon et al. (2009) presented a method focused on dark albedo regions, limiting the scope of the study. Määttänen et al. (2009) also used the continuum at the wavelength 1 μm to retrieve the dust optical depth at specific observations where OMEGA storms were detected. More recently, Leseigneur and Vincendon (2023) used the 2 μm CO_2 band to retrieve dust optical depth over most of the planet and three Mars Years (MY), MY 27–29, providing a global view of dust variations. The 2 μm CO_2 absorption band is, however, sensitive to dust but also to surface pressure and albedo (Forget et al., 2007), which can produce biases in dust retrievals (Leseigneur & Vincendon, 2023).

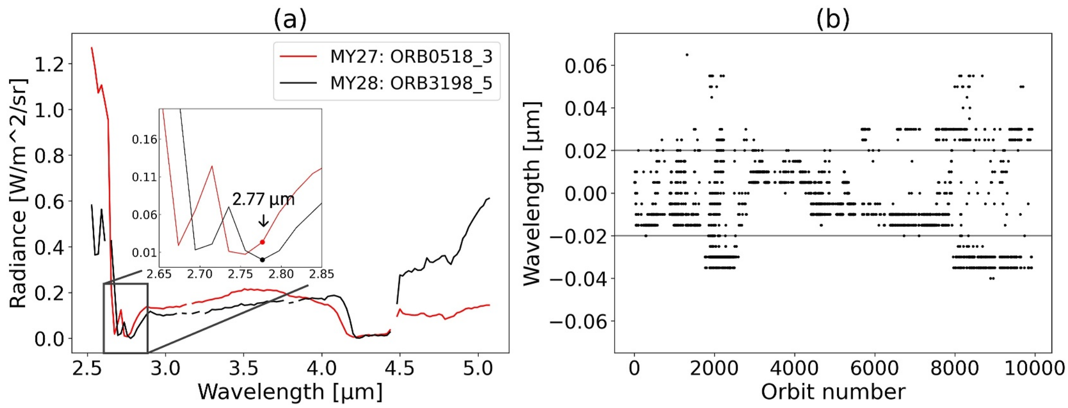

Figure 1. Overview of the OMEGA L-channel spectral shift issue detected in this study. (a) Two observations of the same area observed under similar photometric conditions (see text for details) but for different Martian years are compared. A spectral shift of approximately one spectral pixel is highlighted. (b) The temporal variation of the characterized spectral shift for approximately seven and a half years. The solid line corresponds to the OMEGA wavelength resolution of 0.02 µm (equivalent to one pixel).

Here, we utilize observational data from OMEGA during MY27-29 to obtain dust optical depth based on the opaque CO_2 absorption band at 2.77 µm (Titov et al., 2000). The unique aspect of utilizing 2.77 µm is that the atmospheric dust optical depth can be retrieved independently of surface conditions. Furthermore, this 2.77 µm method is highly sensitive to dust at higher altitudes, allowing for the monitoring of vertically developed dust storms. We first present how we implement this approach and discuss its specific features, which are notably related to its sensitivity to the vertical distribution of dust. Then, by leveraging this novel approach, we conducted a statistical study of LDS over 3 years on Mars, examining their locations, frequencies, and timing of occurrence, including the global dust storm that occurred in MY28.

2. Development of a Dust Optical Depth Retrieval Method Using 2.77 µm Radiance

2.1. Data Set

2.1.1. OMEGA/Mars Express

In this study, we used the near-infrared imaging spectrometer OMEGA onboard MEx to begin its observation on the Martian orbiter in early 2004. OMEGA observes the 0.36–5.09 µm spectral range with three channels (V: 0.36–1.0 µm, C: 0.95–2.65 µm, L: 2.55–5.09 µm), with spectral resolutions of 7 nm, 13 nm, and 20 nm, respectively (Bibring et al., 2004). The C-channel ceased operations in August 2010, after approximately three Martian years of observations, covering the Ls = 330° of MY26 to Ls = 135° of MY30 period, including a global dust storm during MY28. In 2024, the V-channel still performs regular observations while the L-channel conducts limited observations, due to its precarious health. The spatial resolution of OMEGA observations typically varies from ~400 m/pixel to ~4 km/pixel depending on the MEx altitude (elliptical orbit), with coverage of approximately 20° in latitude and ~0.1–~5° in longitude per observation. Due to its high spatial resolution and coverage, OMEGA can observe local scale variations with spectroscopic information. The absolute radiometric accuracy of OMEGA is estimated to be within 10%–20% across its channels (Bonello et al., 2003; Vincendon et al., 2015).

In this study, we retrieved dust optical depth using the radiance measured at 2.77 µm in the L-channel of OMEGA. This wavelength is located near the edge of the L-channel wavelength range. It corresponds to the opaque atmospheric CO_2 band and thus to a very low signal at the bottom of the band. Consequently, its use has been very limited so far. While developing our method, we identified a new artifact in the wavelength calibration of the L-channel data. This artifact remains unnoticed so far as its impact is limited to other uses of L-channel data. A method to correct this wavelength calibration artifact is summarized in the next section (Section 2.1.2).

2.1.2. Correction of the Wavelength Calibration of the OMEGA L-Channel

We identified a new artifact caused by a variable wavelength shift that may be related to other known instrumental issues of the L-channel (Jouglet et al., 2009). We illustrate this artifact in Figure 1 with a typical case. Figure 1a

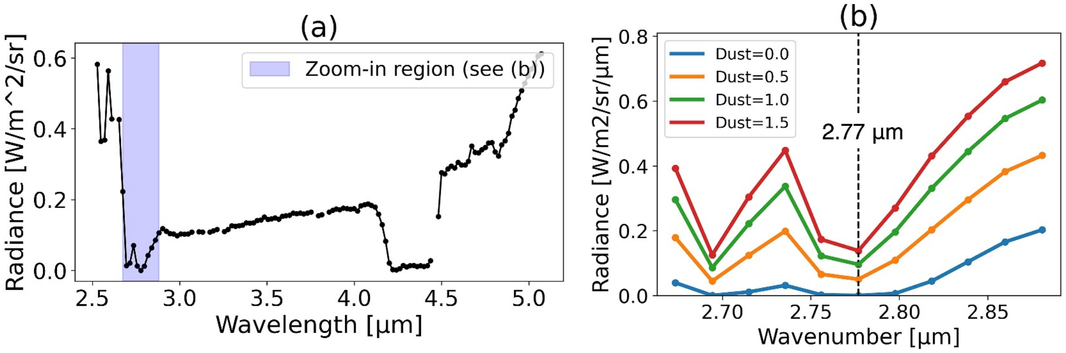

Figure 2. (a) Example of OMEGA observed spectra at L channel. The shaded blue region (2.67–2.9 μm) highlights the spectral range shown in panel (b). (b) Simulated spectra around 2.77 μm for different dust optical depths (0.0, 0.5, 1.0, and 2.0), computed by a radiative transfer model under nadir geometry.

shows the spectra for different years observed under similar conditions. The red data were obtained at Ls = 48° in MY27 (ORB0518_3), with an incidence angle of 56° and an emergence angle of 6°. The black data were obtained at Ls = 76° in MY28 (ORB3198_5) with an incidence angle of 49° and an emergence angle of 8°. The spectrum was shifted by approximately one pixel in the wavelength grid. This shift varies from one observation to the next in a manner that is not currently predictable. Therefore, we developed an empirical method to correct this spectral calibration issue by comparing measured spectra with synthetic spectra.

We first calculated six synthetic spectra by varying the surface pressure (100, 350, 600, 850, 1,100, and 1,350 Pa) without convolution by the OMEGA spectral resolution. Next, the surface pressure values predicted by the Mars Climate Database version 6.1 (MCD v6.1, Forget et al., 1999; Millour et al., 2022) were extracted for each spectrum to select the most appropriate synthetic spectrum. We then calculated a set of spectra by convolving the chosen synthetic spectrum at the OMEGA spectral resolution and changing the spectral grid, adding ±0.005 μm, ±0.01 μm, ±0.015 μm… to the original grid. Finally, we quantitatively evaluated the amount of spectral shift by searching for the highest correlation factor between the synthetic spectra with the different spectral grids and each observed spectrum in the spectral range between 2.65 and 2.8 μm. Figure 1b illustrates the temporal variation in the derived spectral shift over approximately seven and a half years (from ORB0006 to ORB9917). Shifts are typically lower or equal to one spectral pixel in most cases but can reach two or three pixels (Figure 1b). We used the derived spectral shift to determine a new wavelength grid, thus resolving this issue.

2.2. The Dust Optical Depth Retrieval Algorithm

2.2.1. Outline of the Retrieval Procedure

We developed a new method to retrieve the dust optical depth using the radiance measured at 2.77 μm by OMEGA. This wavelength corresponds to the center of the strong absorption band of CO_2 that is typically opaque for nadir-viewing observations on Mars (i.e., no surface signal is detected). However, when aerosols are lifted into the atmosphere, some sunlight is scattered by the aerosols, leading to non-zero radiance. Under the assumption that the vertical mixing ratio of dust is uniform, this can be used to estimate the total optical depth of dust.

Figure 2 shows an example of an OMEGA spectrum and synthetic spectra around 2.77 μm in nadir view, assuming different total optical depths of dust. The synthetic spectra were computed using DISORT (Stamnes et al., 1988) implemented in the ARS code (Ignatiev et al., 2005) with typical OMEGA observation conditions (incidence angle of 52°, emergence angle of 8°, phase angle of 60°) and Mars conditions (surface pressure of 850 Pa, and surface albedo of 0.1) with a uniform vertical mixing ratio of dust. Figure 2 demonstrates a reasonable correlation between the radiance around 2.77 μm and dust optical depth under sufficient atmospheric pressure.

For fast retrieval calculations, we employed a look-up-table method in which a large number of synthetic spectra are calculated in advance for tabulated grid values of physical parameters (e.g., Forget et al., 2007; Toigo et al., 2013), which allows us to instantaneous retrieve dust optical depth. A description of the look-up-table method is presented in Section 2.2.3.

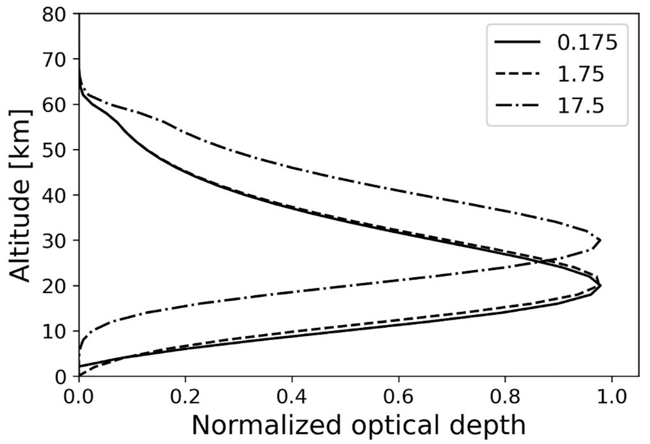

Figure 3. Weighting function in altitude of the radiance at 2.77 μm measured by OMEGA Nadir viewing. Three cases for column optical depths of dust of 0.175, 1.75, and 17.5 are shown.

2.2.2. Radiance Sensitivity to Altitude

As shown in Figure 2, some radiances can be observed at 2.77 μm when dust presents a certain abundance. To know from which altitude these radiances come from, we calculated the weighting functions shown in Figure 3. These weighting functions are calculated assuming that dust number density D(z) (cm^{-3}) at altitude z km is exponentially decreasing with altitude direction, as described by Equation 1:

$$D(z) = D_0 \exp\left(-\frac{z}{H}\right), \tag{1}$$

where D_0 [cm^{-3}] is the dust number density at the surface, and H [km] is the scale height. In this case, the scale height is set as 10 km, a typical value for the Martian atmosphere (Lemmon et al., 2004). The weighting functions are calculated for three different total dust optical depth conditions ($\tau = 0.175$, $\tau = 1.75$, $\tau = 17.5$).

Figure 3 demonstrates that the 2.77 μm radiance comes from an altitude of approximately 30 km, a value that is not significantly modified by changing the optical depth. This is a relatively high value, which corresponds to three scale heights. The sensitivity is reduced by 80% at 10 km (one scale eight). The low sensitivity to the low altitude is due to the opaque CO_2 absorption. As a consequence, most of the dust located below 10 km contributes negligibly to the measured signal. This point will be of importance for the discussion: if dust is well-mixed, extrapolation is straightforward, and measuring the top part of the profile provides access to the full column; however, if the upper part of the vertical profile is more complex (e.g., Conrath, 1975 or Heavens et al., 2011a, 2011b, 2011c with detached layers), the extrapolation becomes an issue.

2.2.3. Look-Up-Table (LUT) Method

The LUT stores the radiance at 2.77 μm calculated by the radiative transfer model, including the effects of multiple scattering, ARS/DISORT, for the tabulated grid values listed in Table 1. There are eight physical parameters in the LUT: surface pressure, temperature, observation geometry (incidence, phase angle, emergencies), surface albedo, and dust optical depth. By performing multidimensional linear interpolation among the parameters within the LUT, the dust optical depth under arbitrary conditions can be retrieved at little computational cost.

The radiative transfer calculation includes absorption due to CO_2 and scattering/absorption due to dust in the atmosphere. The CO_2 line parameters were obtained from HITRAN2020 (Gordon et al., 2022). The absorption coefficient was calculated using a wavenumber resolution of 10^{-2} cm^{-1}. The lower Martian atmosphere (0~60 km) was modeled using 30 plane-parallel atmospheric layers with a uniform CO_2 mixing ratio of 0.953. For the dust optical properties such as single scattering albedo (SSA), extinction cross section, and phase function, we used data based on the work of Wolff et al. (2009), assuming an effective radius of 1.2 μm.

Table 1
Parameters Considered in the Look-Up Table of the Synthetic Spectra at 2.77 μm

Parameters	Symbols	Values	Interpolation function
Surface pressure (Pa)	SP	100, 350, 600, 850, 1,100, 1,350	Linear ln (SP)
Incidences (deg)	IA	0, 15, 30, 45, 60, 75	Linear exp (−cos (IA))
Emergencies (deg)	EA	0, 5, 10, 30	Linear exp (−cos (EA))
Phase angle (deg)	PA	70	(fixed)
Temperature at 0.1 scale height (K)	T_A	160, 213, 260, 285	Linear ${T_A}^{1.5}$
Temperature at 4 scale height (K)	T_B	100, 146, 200	Linear ${T_B}^{1.5}$
Surface albedo	albedo	0.2	(fixed)
Dust optical depth (reference wavelength is 2 μm)	τ	0, 0.3, 0.6, 0.9, 1.2, 1.5, 2.0, 3.0, 5.0, 7.0, 10.0	Linear

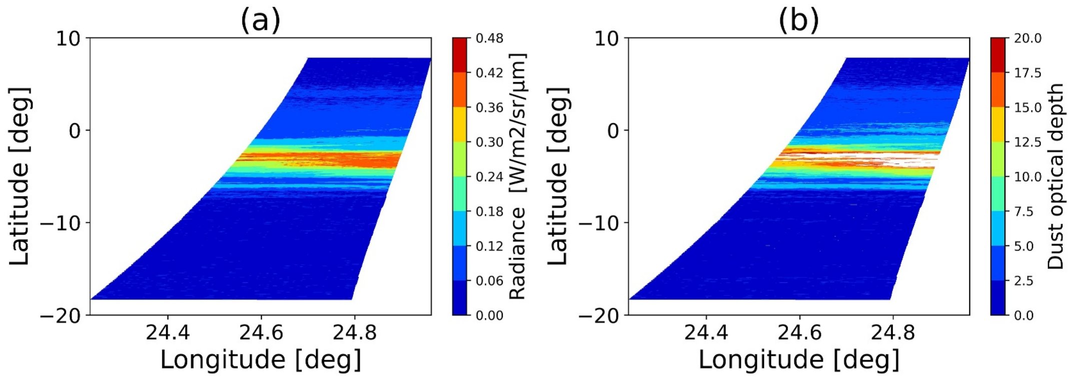

Figure 4. An example of the conversion from radiance at 2.77 μm (a) to the retrieved dust optical depth at 2.0 μm (b) in ORB1212_3 using LUT. OMEGA "rocket dust" storm features are seen at ∼3°S.

To retrieve the dust optical depth using the LUT, the other seven parameters are treated as fixed values. Observation geometry comes from the orbiter data with a precision of around 10^{-3} rad. Surface pressure and temperature profiles are predicted by the Mars Climate Database version 6.1 (MCD v6.1, Forget et al., 1999; Millour et al., 2022), knowing the spatial coordinates, Martian year, solar longitude, and local time position of the observations. The temperature profile is parametrized by one point located at 0.1 scale height above the surface (T_{A}) and then 4 scale heights above the surface (T_B). The temperature is assumed to decrease linearly from T_A to T_B and remains constant beyond T_B (Forget et al., 2007). This is a simplification proposed by Forget et al., 2007, which accounts well for the temperature profile. Because the contribution of the light reflected by the surface to the radiance at 2.77 μm is small, surface albedo is assigned as a fixed value. We also use a representative phase angle (70°) of the OMEGA data set for the calculation as this parameter does not affect the observed radiance. Indeed, both contributions in dust optical depth retrievals are less than 1% when surface albedo and phase angle vary from 0.05 to 0.95 and from 0 to 180°, respectively. This is attributed to the fact that 2.77 μm corresponds to the opaque absorption band of CO_2, allowing the dust optical depth to be estimated independently of the reflective characteristics or conditions of the Martian surface. . The vertical distribution of the dust mixing ratio assumes uniformity in each atmospheric layer from the surface to 60 km altitude. The dust vertical profile is represented by an exponential decay function of the form exp(−h/H), where H is the scale height and h is the altitude. The scale height is calculated as $H = (\mathrm{R^*T})/\mathrm{g}$ using the specific gas constant $R = 192.0$ J kg^{-1} K^{-1}, gravitational acceleration $g = 3.72$ m s^{-2}, and the temperature T at a height corresponding to the 0.1 scale height above the surface. In total, the LUT contains 8,640 calculated spectra corresponding to the parameters listed in Table 1.

Figure 4 shows an example of the dust optical depth retrieval from the observed radiance. This orbit (ORB1212_3) is known to contain a rocket or "OMEGA" dust storm (Määttänen et al., 2009; Spiga et al., 2013; Vincendon et al., 2007). The retrieved map of dust optical depth shows good agreement with the previous study (Määttänen et al., 2009, Figure 4) particularly in the spatial distribution and relative magnitudes. For example, both maps indicate higher optical depth values near the equatorial region. This supports the applicability of our method to dust retrieval. The blank areas in Figure 4 indicate regions without data. They are due to high temperatures in the upper atmosphere (T_B exceeding 200K), caused by dust storms, which triggered exclusion criteria and prevented successful retrieval.

2.3. Evaluation of Uncertainty Sources

We identify six sources of uncertainties in the retrieved dust opacity: (a) assumed atmospheric temperature, (b) assumed atmospheric pressure, (c) instrumental noise, (d) radiometric calibration (e) assumed dust optical properties, and (f) assumed dust vertical profile. Among these errors, the purely random component is (c) and the purely systematic one is (d). For the other errors, they may act both as systematic and random. We assume the same optical property for all of the data (or, assume temperature/pressure from MCD is correct; well-mixed vertical profile for dust). These assumptions might be valid for certain spatial and/or temporal scales (where they act as a source of systematic error) but not for larger spatial and temporal scales in the OMEGA data set (where they can be random for some extend and systematic for some extend).

Table 2
Five Dust Conditions Were Used for Random Error Evaluation

	Orbit number	Latitude	Longitude	Solar longitude	Incidence angle	Emergence angle	τ	Surface pressure	T_A	T_B
(1)	ORB1508_5	12°S	85°E	179°	27°	5°	0.3	401 Pa	226 K	161 K
(2)	ORB1221_5	35°S	139°W	137°	58°	8°	1.2	443 Pa	201 K	158 K
(3)	ORB4661_5	9°S	28°E	299°	35°	2°	2.7	512 Pa	219 K	175 K
(4)	ORB4558_4	13°N	70°E	282°	40°	1°	3.9	555 Pa	217 K	188 K
(5)	ORB4588_4	5°S	3°E	287°	25°	3°	6.6	662 Pa	226 K	187 K

Note. The dust optical depth (τ) is the retrieved value at 2.77 μm.

Given in this complexity, we evaluate these six individual sources of uncertainty independently (described in Section 2.3.1–2.3.6) but do not combine all of the errors. Instead of calculating a global error value by assuming their propagation, we rely on comparisons with a previous study for assessing practical error values (Section 2.4).

In Section 2.3.1–2.3.6, the evaluation of each error was conducted using the five OMEGA data where dust optical depth was previously derived from OMEGA observations using another method (Vincendon et al. (2009): (1) $\tau_{2.0\mu m} = 0.3$, (2) $\tau_{2.0\mu m} = 1.2$, (3) $\tau_{2.0\mu m} = 2.7$, (4) $\tau_{2.0\mu m} = 3.9$, and (5) $\tau_{2.0\mu m} = 6.6$. The details of the five locations are shown in Table 2.

2.3.1. Sensitivity to Near-Surface Atmospheric Temperature

In the retrievals, atmospheric temperatures are obtained from MCD v6.1, which has a spatial resolution of several hundred kilometers, which might significantly deviate from the true local temperature in a pixel of at least a few kilometers. A comparison between surface temperatures derived from the thermal part of the OMEGA spectra and an older version of the MCD shows that temperature discrepancies are generally below 10 K for most of the OMEGA observations (Forget et al., 2007; Jouglet et al., 2007).

To assess the error in the retrieved dust abundance due to the uncertainty in temperature, dust retrievals were performed by shifting the temperature profile by up to ±10 K. Figure 5a shows the difference in the retrieved dust optical depth for the five cases as a function of the difference in assumed temperature. The optical depth difference increases nearly linearly with the temperature difference. They show that the uncertainty is ∼0.12 at a temperature of ∼225 K (cases (1) and (5)), ∼0.08 at ∼215 K (case (4)), and ∼0.04 at ∼200 K (cases (2) and (3)).

2.3.2. Sensitivity to Atmospheric Pressure

Atmospheric pressures are also obtained from the values of the MCD v6.1. Mars is known to have diurnal variations in local atmospheric pressure of ∼5% due to thermal tides (Banerdt et al., 2020). Furthermore, it has been observed that the surface pressure changes by ∼10% during dust storms (Banfield et al., 2020). To assess the impact of changes in local atmospheric pressure due to dust storms on the dust retrieval, we artificially increased and then decreased the atmospheric pressure by up to ∼10% corresponding to 50 Pa of the surface pressure. As the evaluation for atmospheric temperature sensitivity, this analysis was also conducted under the same five cases shown in Table 2.

Figure 5b shows the differences in dust optical depth in these five cases. As for the effect of atmospheric pressure, the differences in retrieved optical depth are larger when the prescribed dust optical depth is used (cases (2) to (5)), except in the very low-pressure case (1), which also corresponds to large optical depth differences. This results in an error margin of up to approximately 0.5. The effect of atmospheric pressure uncertainty diminishes at high surface pressures (∼450 Pa or more), and the error increases with the dust optical depth.

2.3.3. Sensitivity to Instrumental Noise

The raw data of OMEGA are provided in digital numbers (DN) and converted into radiance using the calibration tool (SOFT10) provided by the OMEGA instrument team. The raw data includes a statistical noise of ∼1.85 DN (Forget et al., 2007). The DN at 2.77 μm are usually ∼10 when the dust optical depth is thin (τ is less than 0.5). Thus, statistical noise significantly affects the dust optical depth retrieval. For evaluation, we generated pseudo

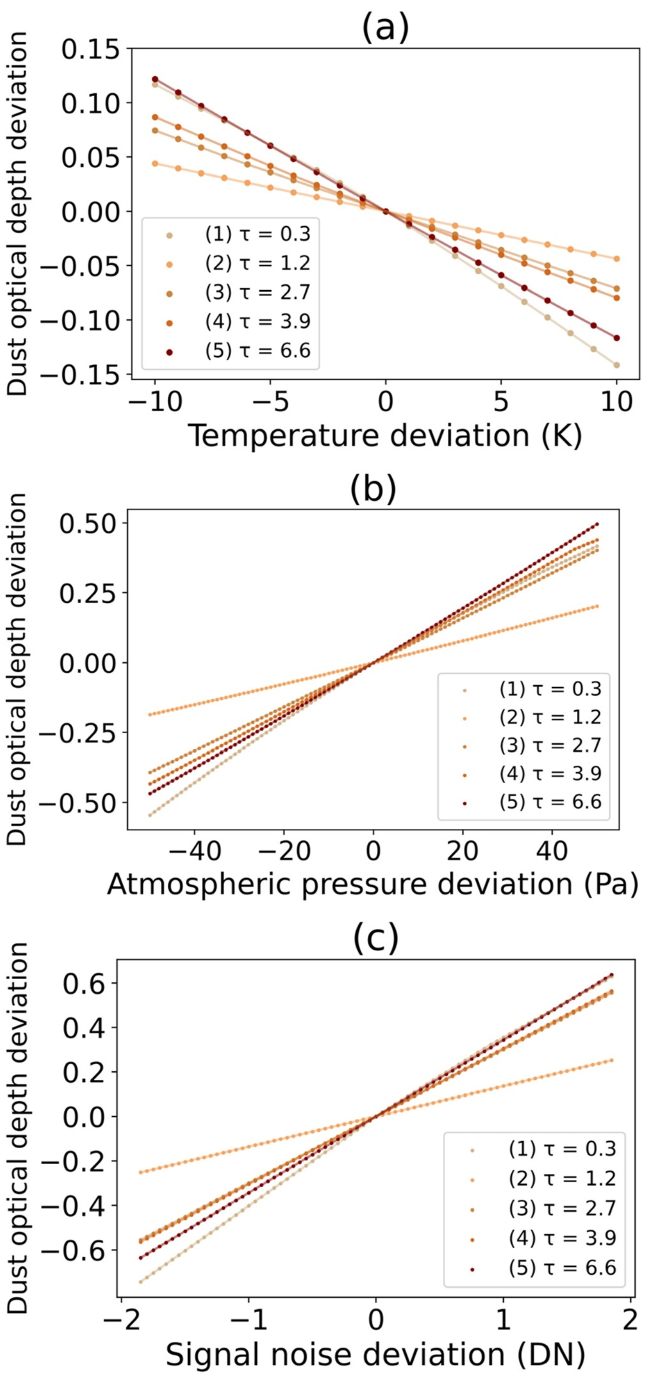

Figure 5. The relative difference of retrieved dust optical depth from the five OMEGA spectra with different prescribed optical depth cases shown in Table 2, associated with (a) temperature errors of ±10 K with an interval of 1 K, (b) surface pressure errors of ±50 Pa with an interval of 1 Pa, and (c) instrumental noise of ±1.85 digital numbers (DN) with an interval of 0.05 DN.

raw data with a ±1.85 DN variation and converted it into a radiance unit (W/m^2/sr/μm) using the SOFT10 tool and investigated the random noise effect on dust retrieval for the five locations shown in Table 2.

Figure 5c shows the difference in the dust optical depth in these five cases. The results are summarized in Table 3. The errors in the retrieved dust optical depth due to the instrumental noise are between 0.25 and 0.75, which is relatively large compared to the other sources. This is expected as the signal at 2.77 μm is extremely low due to absorption by CO_2. The instrumental noise is therefore one of the main sources of errors in the retrieval. We note that this error is estimated for a single pixel, and thus, averaging multiple pixels allows reducing the error. One of the major targets of this study, LDS, is generally spread over more than ∼500 pixels, which gives some flexibility for finding the right trade-off between spatial resolution and optical depth uncertainty.

2.3.4. Sensitivity to Radiometric Calibration

We also evaluated the potential impact of radiometric calibration errors of OMEGA. This type of error can be considered a systematic error, which may affect the retrieval results. The observed signals at 2.77 μm in the OMEGA L-channel typically range from 1 to 50 DN. Thus, even if there is a radiometric calibration error of about 10%–20%, the absolute difference would be limited to about 5–10 DN. The influence of such radiometric errors on the retrieved dust optical depth is illustrated in Figure 5c. For instance, in the case of (5) $\tau = 6.6$, the observed signal is about 40 DN, and a ∼20% error corresponds to ∼8 DN. This would lead to an uncertainty in the dust optical depth of about 2.8. Additionally, in the case of (2) $\tau = 1.3$, the observed signal is about 10 DN, and a ∼20% error corresponds to ∼2 DN, leading to an uncertainty in dust optical depth of about 0.25.

2.3.5. Sensitivity to Dust Optical Properties

A systematic error due to the assumed dust optical properties may also exist. In this study, we used the wavelength-dependent extinction cross section, SSA (SSA), and scattering phase function shown by Wolff et al. (2009) as the dust optical properties in the Martian atmosphere. These data are based on observations from CRISM on board the Mars Reconnaissance Orbiter, which provides a detailed assessment of how Martian dust aerosols scatter and absorb light across different wavelengths. However, it should be noted that absolute calibration differences exist between CRISM and OMEGA, which implies that CRISM-derived optical properties may not always be suited for OMEGA data analysis (Wolff et al., 2019).

The Wolff et al. (2009) study has examined the characteristics of dust optical properties at particle sizes of 1.2 μm, 1.4 μm, 1.6 μm, and 1.8 μm. Here, we assume a constant dust particle size of 1.2 μm at all altitudes, longitudes/latitudes, and seasons for retrieving dust optical depth. However, it is generally known that dust particle size can vary with season or location (Wolff & Clancy, 2003) and tends to decrease with altitude (e.g., Liuzzi et al., 2020). To evaluate the impact of our simplified assumption, a sensitivity test was conducted based on the particle size variations reported by Wolff et al. (2009). Specifically, radiative transfer calculations were performed using the optical properties of dust corresponding to particle sizes of 1.2 and 1.8 μm. Under identical dust optical depth conditions, the radiance difference at 2.77 μm between these two particle sizes was found to be 0.0002 W/m^2/sr/μm. Converting this radiance difference into dust optical depth revealed a difference of only 0.001, which corresponds to an impact of less than 1%. These findings demonstrate that the variability in particle

Table 3
Summarize Retrieval Errors From Temperature, Surface Pressure, and Instrumental Noise for Five Dust Conditions Shown in Table 2

		(1) $\tau = 0.3$	(2) $\tau = 1.2$	(3) $\tau = 2.7$	(4) $\tau = 3.9$	(5) $\tau = 6.6$
Atmospheric Temperature	+10 K	−0.14	−0.044	−0.071	−0.080	−0.12
	−10 K	0.12	0.044	0.074	0.087	0.12
Atmospheric pressure	+50 Pa	0.42	0.20	0.40	0.44	0.50
	−50 Pa	−0.55	−0.19	−0.39	−0.43	−0.47
Signal noise	+1.85 DN	0.63	0.25	0.56	0.56	0.64
	−1.85 DN	−0.74	−0.25	−0.56	−0.56	−0.64

size has a negligible effect on the retrieval method used in this study, supporting the validity of assuming a constant particle size for the analysis.

Other systematic effects related to single scattering properties may however have a more pronounced impact. A particular concern is related to the SSA at 2.77 μm which is not yet well understood. This is notably due to the presence of the opaque atmospheric CO_2 band: once absorption reaches saturation in this wavelength range, the observed reflection spectrum no longer contains contributions from the surface, thus preventing evaluation of the SSA using dust covered surfaces (Ockert-Bell et al., 1997). Furthermore, even without total saturation, the separation of scattering and absorption becomes challenging in regions with extreme CO_2 absorption, and the signal significantly diminishes leading to a degraded S/N. Wolff et al. (2009) thereby reported a lack of observational data in the 2.65–3.0 μm range. However, SSA is expected to vary strongly in this spectral range due to the presence of a hydration band whose shape, and depth are poorly constrained (Määttänen et al., 2009; Wolff et al., 2019). The SSA value we use at 2.77 μm, extracted from the Wolff et al. (2019) data set, is about 0.79, which corresponds to a relatively absorbing dust (for comparison, SSA is ~0.97 in the nearby continuum at 2.5 μm). The use of a higher value of SSA will result in lower retrieved optical depths (as a given radiance could be explained by a lower amount of such brighter dust). We further discuss this point in the upcoming Section 2.4.

2.3.6. Sensitivity to Dust Vertical Profile

Uncertainty in the vertical distribution of dust can significantly affect errors in the retrieved dust optical depth. In this study, we assumed an exponential decay in the dust number density vertical distribution, considering it to be well-mixed. CO_2 gas absorption is more sensitive than the dust amount at 2.77 μm (see Section 2.2.2), making the altitude at which dust is located crucial.

To evaluate its impact, we performed a test: we first calculated radiances simulated for OMEGA data at 2.77 μm with five non-well-mixed dust vertical profiles and then made the retrievals with the simulated radiances assuming the well-mixed profile. For this test, we selected five cases from MY36 (a typical Martian year) at the Curiosity site using MCD v6.1, which include both relatively clear and dusty atmospheric conditions (Cases 1, 2, 3, and 4) and a special case in which a detached dust layer is enhanced around an altitude of 30 km as reported by Heavens et al. (2011a, 2011b, 2011c) (Case 5). The vertical profiles of dust number density scale to a total optical depth of 1.5. Figure 6 shows the assumed vertical profiles for simulating OMEGA data and the values retrieved by our method that assumes well-mixed profiles.

The results presented in Figure 6 demonstrate that the retrieved dust optical depth is significantly sensitive to the vertical distribution of dust particularly in cases where a strong detached layer is located at high altitudes (e.g., around 30 km, Case 5). Under this condition, the retrieved total optical depth can increase by a factor of up to ~2. Conversely, in cases where the vertical profile deviates from the assumed scale height and dust is concentrated predominantly near the surface, the optical depth can be underestimated by a similar factor. However, moderate enhancements at mid-to high-altitudes (e.g., 20–30 km) lead to minimal differences in the optical depth, indicating that the retrieval remains relatively stable under typical atmospheric conditions. As discussed, the uncertainty due to assuming a well-mixed vertical profile of dust is relatively large. However, this method is still valid for detecting a strong LDS that has a large contrast of dust optical depth (see Section 4.1).

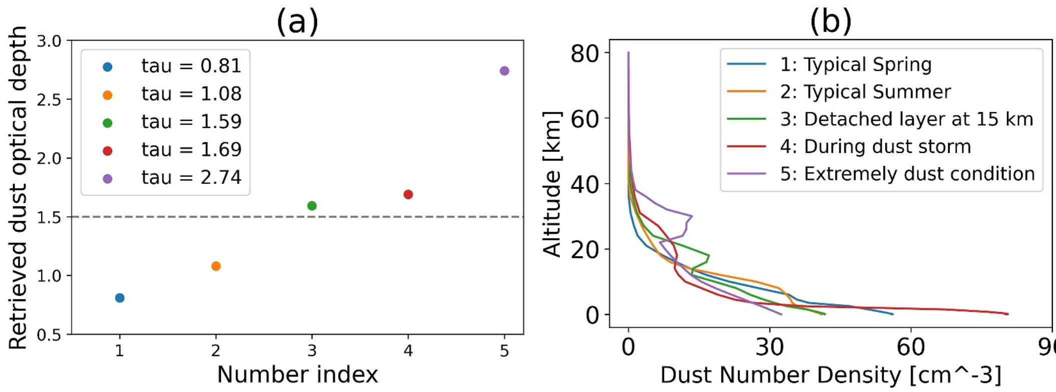

Figure 6. The impact of differences in dust vertical distribution on the retrieved dust optical depth from 2.77 μm. (a) Retrieved dust optical depth values for a given radiance of 0.0110, 0.0147, 0.0217, 0.0231, and 0.037, and different assumed dust vertical profiles. (b) Assumed vertical distributions of dust used in the retrievals. The different colors in panel (a) correspond to different cases. In panel (b), the purple line represents an extreme case with a strong detached layer at 25 km. It was found that the presence of a detached layer above 30 km led to a difference of up to a factor of two in the retrieved dust optical depth compared to cases without.

2.4. Comparison With Another Method

The validity of our method for dust retrieval from the 2.77 μm CO_2 absorption band was assessed by comparing it with a study made by Vincendon et al. (2009). In their study, dust optical depth was retrieved from continuum spectral slopes of OMEGA observations above dark regions using a radiative transfer model. Results were compared to Mars Exploration Rover measurements at a wavelength of 0.88 μm (Lemmon et al., 2004) considered to be a reliable "ground truth" reference. They analyzed data spanning over two Martian years from early 2004 to early 2009, focusing on the areas with a surface albedo (at 1 μm) being less than 0.15 and spatially homogeneous at the low-to-mid-latitudes.

Figure 7 compares our retrieved dust optical depths with the those derived by Vincendon et al. (2009) over the same area and with the same OMEGA observations. We would like to note that our values are the those averaged over 100 pixels around the pixel used by Vincendon et al. (2009) to eliminate the random error due to instrumental noise. The x-axis represents the dust optical depth retrieved by Vincendon et al. (2009), and the y-axis represents our averaged dust optical depths computed at 2.0 μm but converted to the equivalent optical depth at 0.88 μm using the ratio of the extinction coefficients and applying the following equation (the multiplicative factor is derived from Wolff et al., 2009 dust optical properties):

$$\text{Dust Optical depth}_{0.88\ \mu\text{m}} = \text{Dust optical deph}_{2.0\ \mu\text{m}} \times 1.12$$

From this comparison, we can estimate the magnitude of the practical errors in our retrievals. The best-fit linear function of the comparison is $y = 2.1x$ - 1.1, where the dust optical depth is retrieved by Vincendon et al. (2009), and y is our result. The comparison suggests that the dust optical depth given using our method could be systematically overestimated by a factor of 2.1 and offset by -1.1. The standard deviation between the best-fit linear function and the individual data point is 0.52, which is a practical error in relative variations.

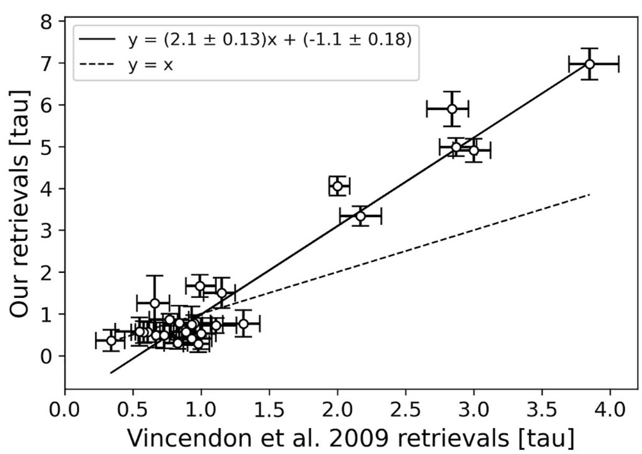

Figure 7. Comparison between the dust optical depth retrieved in this study using the 2.77 μm CO_2 band depth and converted to 0.88 μm (y-axis), and the dust optical depth retrieved at 0.88 μm by Vincendon et al. (2009) using the spectral slope (x-axis). The solid line represents the best linear fit, whereas the dashed line represents the line $x = y$.

The origin of this discrepancy is likely multifactorial, involving all the error sources discussed. However, we highlight that the assumed vertical distribution of atmospheric dust is likely to be one of the dominant sources of the discrepancy. This discrepancy arises because our method is mainly sensitive to dust at higher altitudes particularly around 20–30 km (see Figure 3). In contrast, the method by Vincendon et al. (2009) responds to dust distributed throughout the entire atmospheric column. Retrievals rely on a representative

Table 4
Data Used for Retrieval Selection Criteria

Description	Formulation/Source	Value
Water ice cloud index	R(3.4 μm)/R(3.5 μm)	<0.8
Surface pressure	MCD v6.1	>400 Pa
Surface altitude	MOLA	<+10 km
Incidence angle	OMEGA observing geometry	<60°
Emergence angle	OMEGA observing geometry	<10°
Data quality	OMEGA data (SOFT10)	≥3 (~ORB1900) ≥4 (ORB1900~)

well-mixed vertical profile of dust, and our sensitivity tests using non-well-mixed profiles suggest that the resulting optical depth can vary by up to a factor of ∼2, depending on the assumed structure (see Figure 6). For some observations, the dust optical depth obtained by our method is close to zero, while the one obtained by Vincendon et al. (2009) is around 0.5–1.3. These discrepancies could be thought to result from non-well-mixed vertical profiles. As discussed in Section 2.3.6, if dust is concentrated near the surface, CO_2 absorption may saturate before dust is seen. In contrast, the method used by Vincendon et al. (2009) is sensitive to changes in surface brightness, enabling the detection of dust near the surface. The comparison between these two methods with differing altitude sensitivities suggests that the discrepancies observed in regions with thin dust layers may indicate that the dust is concentrated at low altitudes. By taking advantage of these discrepancies, the two methods could be combined to constrain the vertical profile in the future.

The discrepancy may also be related to the poor knowledge of the 2.77 μm SSA as discussed previously in Section 2.3.5: a higher SSA will decrease the 2.77 μm optical depth and make both values more similar. In addition, Vincendon et al. (2009) show that their retrievals may suffer from systematic biases too, related notably to the assumption regarding the single scattering phase function: the use of another plausible phase function is shown to increase optical depths by 20%–30%, which will also reduce the systematic discrepancy between both values.

3. Application of the Retrieval Method to the OMEGA Data

We applied the developed retrieval method with the opaque CO_2 absorption band at 2.77 μm to the whole OMEGA L-channel (see Section 2) data set and derived the variation of dust optical depth in MY27-29, including the MY28 GDS. In this section, we explain the criteria for data selection and present the seasonal and global-scale variation of the retrieved dust optical depth. Furthermore, we utilize the retrieved dust optical depth to detect LDS on Mars, addressing their spatial distribution and seasonal variations, which are discussed in Section 4.

3.1. Criteria for Data Selection

Table 4 shows the criteria for data selection. With our dust optical depth retrieval method, atmospheric dust and ice clouds have the same effect of increasing the radiance at 2.77 μm. Therefore, data containing water ice clouds were identified and were excluded using the water ice index defined as the ratio between 3.4 and 3.5 μm reflectance (Audouard et al., 2014; Langevin et al., 2007; Madeleine et al., 2012). Additionally, to avoid the data with insufficient CO_2 saturation, the data with the surface pressure predicted by MCD v6.1 being below 400 Pa were excluded. This is because our radiative transfer calculation showed that the radiance at 2.77 μm contains reflected sunlight from the surface when the total pressure is below 400 Pa. For the same reason, data from areas with surface altitudes exceeding 10 km were excluded. However, we also avoid configurations with incidence angles >60° and/or emergence angles >10° as they imply probing a larger air mass and thus higher CO_2 absorption for the same altitude, limiting the sounding depth and thus the capacity to sense the dust layer. Finally, we also performed a selection based on the data quality identified by the OMEGA software SOFT10. The data quality of 3 or higher before ORB1900 and 4 or higher after ORB1900 were used.

3.2. Seasonal Variation of Dust Optical Depth

By applying the criteria shown in Table 4, dust optical depth retrieval was conducted on 4,013 observations ($\sim 4 \times 10^9$ spectra) out of the total 8,375 ($\sim 1 \times 10^{10}$ spectra) observations from the entire observational period of OMEGA in MY27-29. The derived seasonal variation of dust optical depth is shown in Figure 8. The vertical axis represents latitude with longitude averages taken for each degree of latitude (averaging ∼500 pixels). The horizontal axis represents the variation in solar longitude. The seasonal variation of the retrieved dust optical depth is consistent with previous studies (Leseigneur & Vincendon, 2023; Montabone et al., 2015; Smith et al., 2001). The dust optical depth remains low from Ls = 0°–180° in the northern spring-summer period, while it increases after Ls = 180°, which corresponds to the southern spring-summer period. Notably, a significant global increase in the

10.1029/2025JE008987

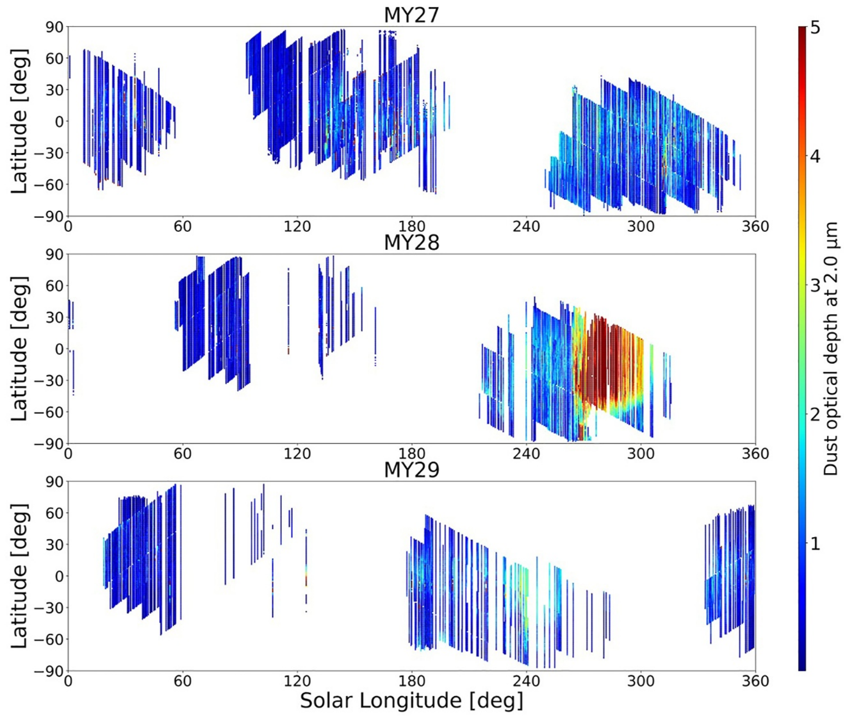

Figure 8. Seasonal variation of the dust optical depth retrieved from 2.77 μm in MY27-29. The reference wavelength of the dust optical depth is 2.0 μm.

dust optical depth was observed after Ls = 270° in MY28, corresponding to the GDS. Additionally, an increase in dust was confirmed during the active dust period (B-storm season) in MY29.

3.3. Global-Scale Variation of Dust Optical Depth at the Initial Phase of the GDS in MY 28

The MY28 GDS is known to have started around Ls = 265°, but the location of its initiation remains uncertain. Previous studies have suggested that potential trigger locations include Chryse Planitia (28.4°N, 319.7°E) and Noachis Terra (44°S, 350°E), but observational data remain insufficient to precisely identify the origin (Wang & Richardson, 2015).

Figure 9 shows the temporal variation of the geographical distribution of dust optical depth just before the onset of MY28 GDS, as observed by OMEGA. Around Ls = 247°–250°, an LDS or RDS with $\tau < 3$ was detected near the equator at ∼−10°E (see Figure 9a). From that point until around Ls = 262°, intermittent and LDS or RDS dust storms with $\tau < 3$ appeared and dissipated particularly near the equator (see Figures 9b–9e). From Ls = 262°, a stronger dust storm with τ exceeding three emerged near the equator at ∼−10°E, followed by a gradual increase in global dust optical depth (see Figures 9f–9h). From Ls = 271°, the dust optical depth had increased globally as a GDS became evident (see Figures 9i–9l. Focusing on just before the MY28 GDS (Ls = 265°), dust storms with τ exceeding three were observed developing around Chryse Planitia and Noachis Terra (see Figure 9f). Subsequently, in Noachis Terra, an even more extensive and thick dust storm with τ surpassing five was detected, while τ around Chryse Planitia decreased to approximately two. Based on only this observation, it is not possible to determine which dust storm developed first. However, future work combining OMEGA data with multiwavelength observations sensitive to different altitudes' sensitivity of dust (e.g., Leseigneur & Vincendon, 2023; Vincendon et al., 2009) should make it possible to estimate the height of the top of these dust storms, enabling a quantitative evaluation of their development processes at both locations.

10.1029/2025JE008987

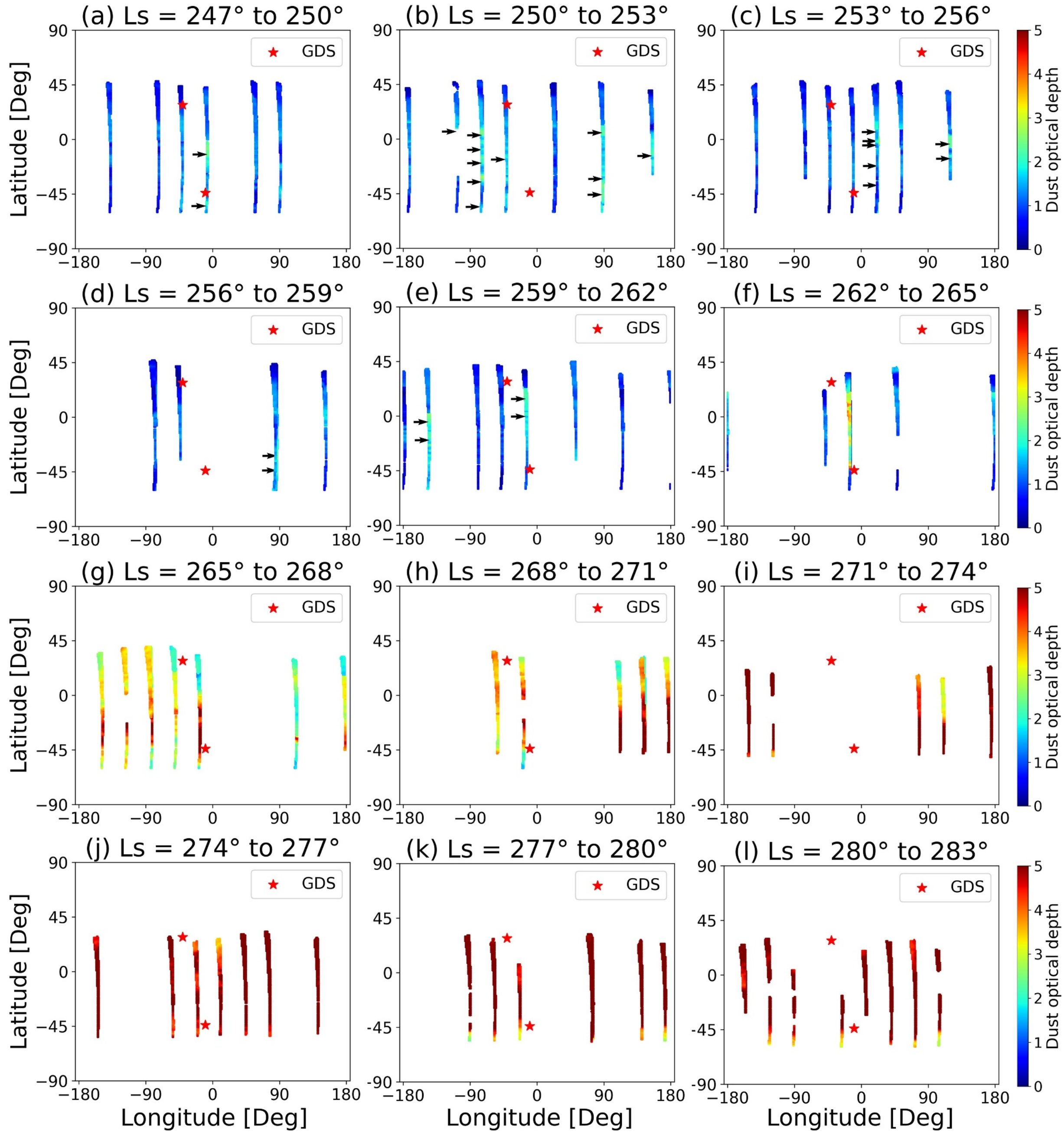

Figure 9. The temporal variation of the geographical distribution of dust optical depth for the period including the onset of MY28 global dust storms (Ls = 247°–283°). Two red stars represent Chryse Planitia (28.4°N, 319.7°E) and Noachis Terra (44°S, 350°E). The global maps of dust optical depth at 2.0 μm for the Ls range of 3° width. Black arrows indicate the approximate locations of regional or local dust storms ($\tau < 3$ region) identified in panels (a–e).

4. A Statistical Study of the Local Dust Storm Occurrences

4.1. Search of Local Dust Storms

From the dust optical depth data shown in Figure 8, we searched for LDS by applying the following method (described in Figure 10). First, a running median with a grid of 1° latitude and 1° longitude was applied to the retrieved pixel-to-pixel dust optical depth to reduce random error. In the second step, we extracted the smoothed data with $\tau > 2$. Finally, as the final step, we identified LDS based on the size of areas where $\tau > 2$. Based on the LDS definition (Cantor et al., 2001), we set the area to be between 1.0×10^4 km^2 and 1.0×10^6 km^2. Observations in which all pixels within a single observation had an $\tau > 2$ were excluded, as the scale of the dust storm could not

10.1029/2025JE008987

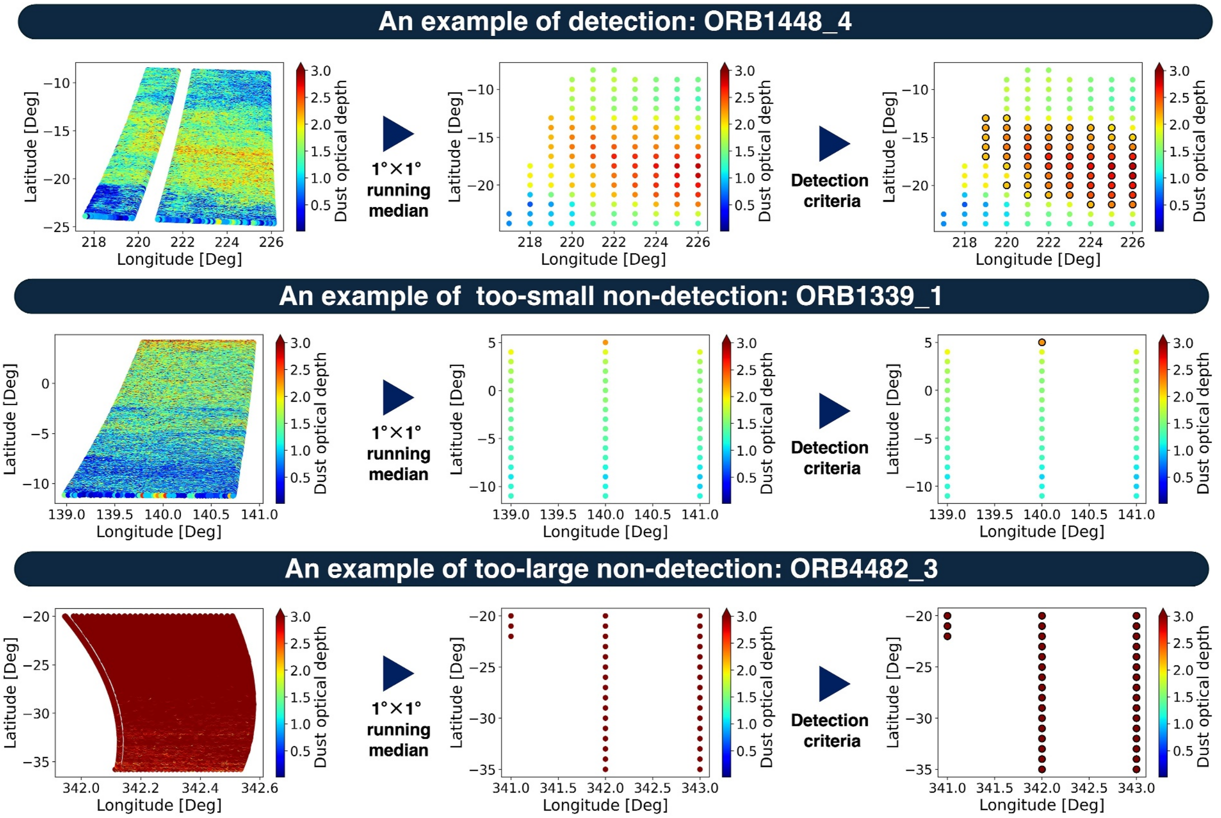

Figure 10. Overview of the Local Dust Storms detection method with three examples of OMEGA observations. The circles surrounded by a black line are the area where $\tau > 2.0$. The third example shows a case where the size of the dust storm cannot be constrained.

be constrained (Figure 10, the third example). This analysis was restricted to latitudes within ±60° to remove the influence of CO_2 ice clouds, which frequently occur in high-latitude regions of Mars (Ivanov & Muhleman, 2001.). Also, due to the limited longitudinal observation range of OMEGA (about 2°–10°), dust storms may be only partially observed, and the detected part may be too small to meet the size criteria. Consequently, some dust storms extending in the longitudinal direction may have been missed due to these field-of-view limitations.

Based on these criteria, 146 LDS were detected between MY 27 and 29, and their seasonal distribution is shown in Figure 11. Two key characteristics were identified within this distribution. The first characteristic is that a cluster of the LDS was detected during Ls = 130°–200° only in MY27. This cluster includes the storm previously identified at Ls = 136° in MY27, as reported notably by Määttänen et al. (2009). It is known that RDS occur annually during this period (Battalio & Wang, 2021), and every few years, they can evolve into large regional RDS, known as "Z storms" (Heavens et al., 2019a, 2019b). In this study, such LDS clusters were not detected in other Martian years, which may be because observations were performed at different local times at each MY and/or the number of observations was much less in MY 28 and 29. Additionally, observations in MY28 were biased toward high northern latitudes, which could account for the lack of detection. Observations by OMEGA in MY27 included local times around 14:00, aligning with previous dust storms database time slots (Battalio & Wang, 2021). In contrast, the MY28 and MY29 observations were concentrated between 6:00 and 8:00 in the early morning potentially making it difficult to detect LDS during that period if they had not yet formed.

The second characteristic is specifically to point out the enhancement at Ls = 240°–330° in MY27, Ls = 210°–310° in MY28 and around Ls = 240°–250° in MY29. The local time of these detections is primarily concentrated between 12:00 and 16:00. This result indicates that the frequency of LDS occurrence is highly dependent on local time. In MY27, LDS were frequently observed during the B and C storm seasons from Ls = 250°–330°. In MY28, numerous LDS were identified from Ls ~270° just before the onset of the GDS. In MY29, several LDS were observed during the A storm season. The reduced number of detections in MY29 is attributed to limited observations during the B and C storm seasons and a concentration of observations in the early morning.

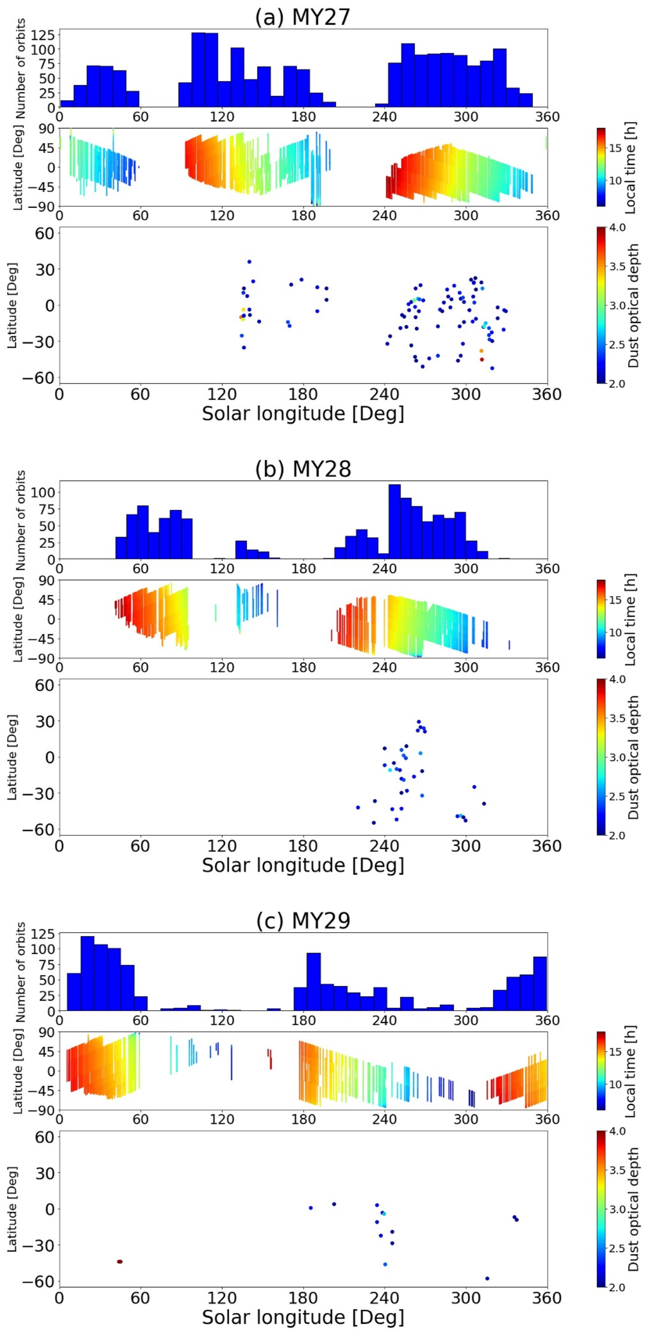

Figure 11. Distribution of OMEGA data coverage and detected Local Dust Storms (LDS) for MY27, 28, and 29. For each MY: (top) The number of orbits during which OMEGA performed observations. (middle) The season-latitude maps of observation local time. (bottom) The season-latitude maps of detected LDS.

Additionally, some of the LDS detected during this season may be portions of dust storms extended in the longitudinal direction, partially observed due to the OMEGA field-of-view limitation, which requires careful interpretation. However, the frequent detection of LDS during the Ls = 180°–360° range suggests that smaller-scale dust storms might occur more frequently just before large-scale dust storms. This may imply that LDS could be the seed that creates larger storms (Cantor et al., 2001; Hinson & Wang, 2010; Martin & Zurek, 1993; Wang & Richardson, 2015). In the following sections, we will discuss the local time dependence of LDS and its geographical distribution for each season.

4.2. Local Time Variation

In this study, we analyzed the probability of LDS occurrence at various local times using OMEGA data (Figure 12). The probability of occurrence was calculated by dividing the total number of LDS detected by the total number of OMEGA observations at each local time. Information on the number of detections and total observations for each period is provided in Table 5. Error bars, based on the number of observations at each time, indicate the 68% reliability of detection. Bins with fewer than 200 observations are displayed with lighter colors to highlight lower confidence. The error bars are calculated using the standard error of proportions, applying the following formula:

$$\text{Error} = \sqrt{\frac{p(1-p)}{n}},$$

where p represents the detection probability, and n is the number of observations.

Figure 12 reveals three key features of the local time dependence of LDS detection: (a) a detection peak at noon during both seasons (around 13:00 for Ls = 0°–180° and 12:00–13:00 for Ls = 180°–360°), (b) a decrease in detection rates during the afternoon, and (c) a secondary peak after 15:00 observed exclusively for Ls = 180°–360°. The characteristics of LDS detection provide insights into the associated phenomena.

The peak in LDS detection at noon suggests that LDS may begin to form around 8–10 a.m. The primary driver of dust storms is atmospheric heating caused by solar radiation, which increases atmospheric temperatures in the morning. This heating leads to vertical transport over several hours, triggering the formation of LDS. Previous modeling studies (Spiga et al., 2013; Wang et al., 2018) have shown that LDS originating near the surface can be transported to altitudes of up to 30 km within 3–4 hr. Furthermore, observational data from the Mars Environmental Dynamics Analyzer onboard Perseverance reported a gradual increase in dust optical depth over Jezero Crater starting at dawn and peaking around noon (Smith et al., 2023).

As for the afternoon decreases in LDS detection rates, two possibilities are considered. First, the decay of LDS could be more plausible during seasons with lower atmospheric dust activities in Ls = 0°–180°. Limited atmospheric activity during this period likely shortens the time for dust lifted to high altitudes to settle back near the surface. On the other hand, during seasons with higher dust activities in Ls = 180°–360°, vigorous convective activity may prolong the suspension of dust in the atmosphere. As a result, there is a less pronounced decrease in detection rates. Second, the evolution of LDS into RDS, as periods of high atmospheric dust activities with vertical convection may sustain suspended dust for extended periods. Observations by the EMM indicate that LDS and RDS activity near the surface peaks occur between 2 and 4 p.m. (Guha et al., 2024). It is approximately 2–3 hr after the

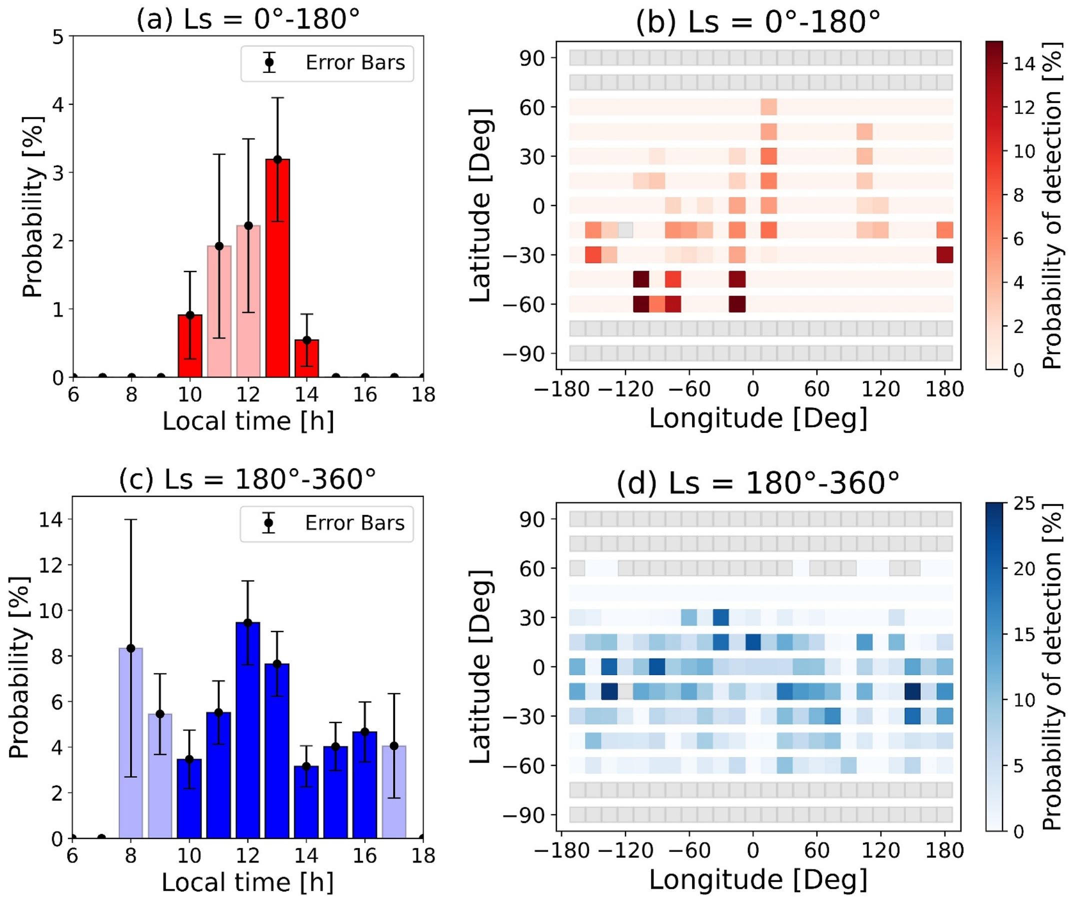

Figure 12. The local time distributions of Local Dust Storms (LDS) for (a) Ls = 0°–180° and (c) Ls = 180°–360°. The interval is 1 hr from 6-a.m. to 6 p.m. Bins with fewer than 200 observations are displayed with lighter colors to highlight lower confidence. The geographical maps of the LDS detection probability for (b) Ls = 0°–180° and (d) Ls = 180°–360°. The gray indicates areas with no observations.

peak at noon observed in this study. This suggests that LDS formed in the morning may evolve into RDS in the afternoon, expanding the storm area and reducing the likelihood of LDS detection, an interpretation particularly plausible during the dust storm season.

The secondary peak observed after 3 p.m. could be explained by three possible speculations. The first is related to the decay of RDS. As the solar zenith angle increases toward the late afternoon, solar radiation decreases. This leads to rapid atmospheric cooling, which may cause RDS to decay and be detected again as LDS. The second involves the re-suspension of dust after storm decay. Following the weakening of LDS and the descent of dust to

Table 5
Number of OMEGA Observations and LDS Detections Each Local Time

Ls = 0°–180°															
Local time (h)	5–6	6–7	7–8	8–9	9–10	10–11	11–12	12–13	13–14	14–15	15–16	16–17	17–18	18–19	19–20
Number of observations	3	3	10	71	138	220	104	135	376	368	472	352	55	4	0
Number of detections	0	0	0	0	0	2	2	3	12	2	0	0	0	0	0
Ls = 180°–360°															
Local time (h)	5–6	6–7	7–8	8–9	9–10	10–11	11–12	12–13	13–14	14–15	15–16	16–17	17–18	18–19	19–20
Number of observations	4	3	17	24	165	202	272	254	353	380	348	257	74	2	0
Amount of detections	0	0	0	2	9	7	15	24	27	12	14	12	3	0	0

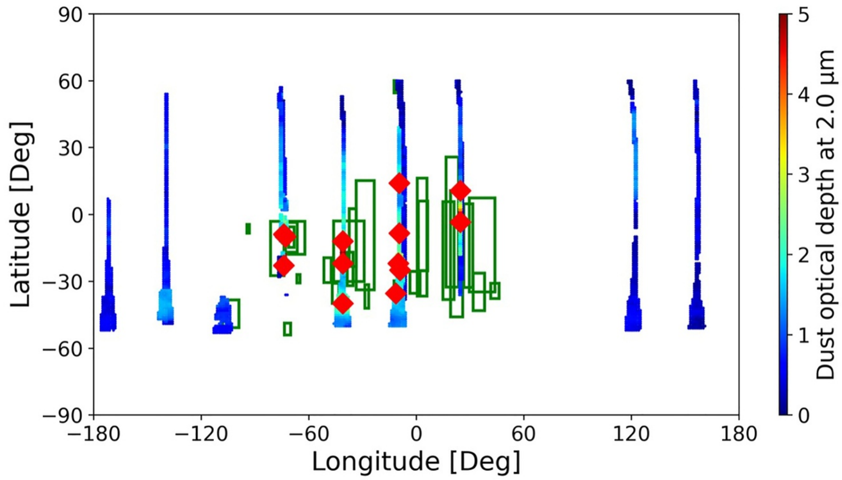

Figure 13. Spatial distribution of the Local Dust Storms (LDS) during the quiet season. Above the OMEGA dust optical depth retrievals (see Section 3) for Ls = 133°–138° in MY27, the red diamonds indicate LDS detected by OMEGA in this study. Green squares symbolize the Mars Dust Activity Database dust storms (Battalio & Wang, 2021) detected in Mars Years 27 during Ls = 133°–138°.

lower altitudes, external factors, such as increased late afternoon winds or temperature gradients, might loft the dust back to higher altitudes, producing a secondary peak. The third suggests that this peak may not correspond to LDS but rather to high-altitude dust layers, such as detached layers: in such cases, our method will result in optical depths biased toward higher values (see Section 2.3.6). Previous observations by Mars Climate Sounder (MCS) have shown that detached layers frequently occur in the late afternoon (Heavens et al., 2011c). While the formation mechanism of these layers remains unclear, the results of this study may indicate a connection to this phenomenon. Further discussion and investigation of these three hypotheses are necessary.

4.3. Spatial Variation

The detection probability of the identified LDS is presented on latitude-longitude maps (Figures 12b and 12d). During the Ls = 0°–180°, LDS detections were concentrated in specific regions mostly in the mid to high southern latitudes (e.g., Cimmeria Terra, Sirenum Terra, Argyre Planitia, Aonia Terra) and close to the northern hemisphere flushing dust storm channels (e.g., Acidalia-Chryse, Utopia-Isidis, see Battalio & Wang, 2021). On the contrary, during the Ls = 180°–360°, the LDS is quite everywhere except in latitudes above 40°N, with some probability peaks in mid-latitudes (e.g., Chryse Planitia, Daedalia Planum, Cimmeria Planum, Tharsis mons).

The LDS-preferred regions identified during Ls = 0°–180° (see Figure 12) were compared with the Mars Dust Activity Database (MDAD) (Battalio & Wang, 2021). This is a dust storm database built from UV-visible global images (MOC/MGS, MARCI/MRO). Figure 13 compares dust storms detected by OMEGA and MDAD. The red diamonds represent LDS detected by OMEGA in this study, whereas the green squares indicate dust storms identified by MDAD. Our results confirm that dust storms have a strong regional preference.

Despite OMEGA observing various regions during this period (Ls = 133°–138°), the detected LDS were concentrated in specific areas. These specific areas include Acidalia-Chryse and Utopia-Isidis, which are part of flushing dust storm channels. Global circulation models have identified these channels as areas with particularly high surface wind stress (Basu et al., 2006; Kahre et al., 2006; Mulholland et al., 2013; Newman et al., 2002; Toigo et al., 2012) and have been recognized in previous studies as frequent sites for dust storm activity (e.g., Battalio & Wang, 2021; Wang & Richardson, 2015).

Typically, during Ls = 180°–360°, the combination of increased temperatures and surface winds creates favorable conditions for dust storm formation (Hinson & Wang, 2010). However, when solar radiation flux is minimal on Mars during the aphelion, there is no significant increase in global temperature. Consequently, the influence of temperature diminishes, and LDS activity could be primarily observed in regions where surface wind stress is exceptionally high. This situation highlights these areas as significant "hotspots" for dust storm activity, emphasizing their importance in understanding Martian atmospheric dynamics.

During Ls = 180°–360°, an increase in detection rates was also observed in regions such as Chryse Planitia and Tharsis mons. These trends align with known areas of frequent larger-scale dust storms (regional and large-local dust storms) observed through previous visible imaging studies (Battalio & Wang, 2021; Wang & Richardson, 2015). Our analysis did not detect LDS north of 40°N during Ls = 180°–360°, even though this region is known for intensified dust storm activity driven by baroclinic waves around Ls ∼181° (Wang & Richardson, 2015). Three speculations could explain why LDS were not detected there.

The first is the influence of meridional circulation. The mid-to-high latitude regions in the northern hemisphere are in the downwelling branch of the meridional circulation. At this season, large-scale atmospheric circulation, notably the Hadley circulation, might confine dust storms to lower altitudes (∼30 km or below) (Bertrand et al., 2020). Observations from the MCS confirm that northern high latitudes greater than ∼40°N are relatively clear sky isolated from the rest of the planet (Heavens et al., 2011a, 2011b, 2011c). This could also suggest that, in this region, vertical motions are not strong enough to transport the dust at the altitude sensibility of our method, leading to the nondetection of LDS.

The second is the influence of surface altitude and solar radiation. On Mars, the northern hemisphere generally has a lower surface altitude compared to the southern hemisphere. Additionally, due to the elliptical orbit and axial tilt, the northern hemisphere receives less solar radiation during Ls = 180°–360°. This means more energy is required to lift dust to high altitudes in the northern hemisphere. Consequently, dust in the mid-high latitude regions may not reach sufficient heights, making it undetectable in our analysis.

The third is the difference in CO_2 abundance. Because the northern hemisphere has a lower surface elevation, it has a higher CO_2 content (higher surface pressure) than the southern hemisphere. In our retrieval method, dust detection relies on a decrease in CO_2 absorption as dust rises, which resolves saturation and enables detection. However, in the CO_2 rich northern hemisphere, the altitude at which saturation is resolved is higher than in the southern hemisphere. This means that even more energy is required for dust to reach detectable altitudes in the mid-to-high latitude regions of the northern hemisphere, reducing the likelihood of LDS detection.

5. Summary and Conclusions

This study investigated the spatial-temporal variability of LDS on Mars using the high spatial resolution and wide coverage of local time of OMEGA onboard MEx.

We developed a new method for the retrieval of dust optical depth using 2.77 μm, which corresponds to an opaque CO_2 absorption band. When dust is sufficiently present at high altitudes above 20–30 km, reflected sunlight from the dust is detectable at this wavelength (see Section 2, Figures 2 and 3). Observed radiance by OMEGA is compared to a look-up table calculated by a radiative transfer model to quickly retrieve the dust optical depth.

By error analysis, we have shown that this method has a relatively large random error in the retrieved dust optical depth (∼0.52 for single spectrum) and possible systematic bias by a factor of ∼2. The former is basically caused by low SNR (instrumental noise) and the latter is due to multiple assumptions such as the vertical profile of optical parameters of dust. These values are relatively large; however, the method is valid for searching LDS that has a strong contrast of optical depth.

This method was applied to the L-channel data of the OMEGA. We applied our analysis to 8,375 observations ($\sim 10^{10}$ spectra) taken in MY27-29. As a result, the dust optical depth was successfully retrieved from 4,013 observations ($\sim 4 \times 10^9$ spectra). Our data set provides the seasonal variation of dust optical depth (see Section 3, Figure 7) and captures changes in global dust distribution before the onset of the MY28GDS (see Section 3, Figure 8).

Furthermore, 146 LDS events were detected (see Section 4, Figure 10). We found remarkable local time dependencies (see Section 4, Figure 11) of the dust optical depth around 30 km altitude: (a) a detection peak around noon (13:00 for Ls = 0°–180° and 12:00–13:00 for Ls = 180°–360°), suggesting LDS initiation around 08:00–10:00; and (b) a declining detection rate in the afternoon, implying LDS dissipation or evolution into RDS. LDS during Ls = 0°–180° were restricted in specific regions such as Chryse Planitia. Only MY27, a frequent occurrence of LDS, was observed during Ls = 130°–150°. On the other hand, LDS during Ls = 180°–360° were distributed over a wide range of latitudes and longitudes, except for latitudes north of 40°N (see Section 4, Figure 11). Notably, the LDS during Ls = 0°–180° were concentrated in regions with high surface wind stress and frequent dust storm activity.

In the future, this method may also be applied to CRISM onboard MRO data, which covers a similar wavelength range to OMEGA and future missions such as MIRS onboard MMX (Barucci et al., 2021; Kuramoto et al., 2022; Ogohara et al., 2022). Moreover, a coordinated study with lower atmospheric dust optical depth by 2.0 μm analysis (Leseigneur & Vincendon, 2023) could enable a more detailed understanding of the dust vertical distribution in the Martian atmosphere. Additionally, using our dust retrievals as input for surface pressure retrieval based on the 2 μm CO_2 absorption (Forget et al., 2007) could potentially improve the accuracy of surface pressure retrieval.

Data Availability Statement

Information on the data set was used for the statistical analysis of LDS based on dust optical depth and is archived by Kazama. (2025). We used the calibrated OMEGA data set archived at the ESA Planetary Science Archive (PSA, 2023) for this study.

Acknowledgments

Akira Kazama is supported by the MEXT WISE Program for Sustainability in the Dynamic Earth. Akira Kazama is supported by Grant-in-Aid for JSPS Fellows (Grant 24KJ0340). Shohei Aoki is supported by JSPS KAKENHI (Grant 22K03709, 22H05151, 22H00164, 22KK0044, and 19H00707). Yasumasa Kasaba is supported by a JSPS KAKENHI Grant-in-Aid for Scientific Research(A) (Grant 19H00707). Thomas Gautier, Yann Leseigneur, Franck Montmessin and Aymeric Spiga acknowledge the financial support of the Centre National d'Etudes Spatiales, France (CNES) through its APR program [Not Available in CrossRef][Not Available in External Pubmed]. Thomas Gautier and Yann Leseigneur acknowledge the financial support from Agence National de la Recherche, France, under the Grant ANR-20-CE49-0004-01. Hiromu Nakagawa is supported by JSPS KAKENHI Grants (Grant 22KK0044, 23H04646, 24K21561).

References

Audouard, J., Poulet, F., Vincendon, M., Milliken, R. E., Jouglet, D., Bibring, J. P., et al. (2014). Water in the martian regolith from OMEGA/Mars express. *Journal of Geophysical Research: Planets*, *119*(8), 1969–1989. https://doi.org/10.1002/2014JE004649

Banerdt, W. B., Smrekar, S. E., Banfield, D., Giardini, D., Golombek, M., Johnson, C. L., et al. (2020). Initial results from the InSight mission on Mars. *Nature Geoscience 2020*, *13*(3), 183–189. https://doi.org/10.1038/s41561-020-0544-y

Banfield, D., Spiga, A., Newman, C., Forget, F., Lemmon, M., Lorenz, R., et al. (2020). The atmosphere of Mars as observed by InSight. *Nature Geoscience 2020*, *13*(3), 190–198. https://doi.org/10.1038/s41561-020-0534-0

Barucci, M. A., Reess, J. M., Bernardi, P., Doressoundiram, A., Fornasier, S., Le Du, M., et al. (2021). MIRS: An imaging spectrometer for the MMX mission. *Earth Planets and Space*, *73*(1), 1–28. https://doi.org/10.1186/s40623-021-01423-2

Basu, S., Wilson, J., Richardson, M., & Ingersoll, A. (2006). Simulation of spontaneous and variable global dust storms with the GFDL Mars GCM. *Journal of Geophysical Research*, *111*(E9), E09004. https://doi.org/10.1029/2005JE002660

Battalio, M., & Wang, H. (2021). The Mars dust activity database (MDAD): A comprehensive statistical study of dust storm sequences. *Icarus*, *354*, 114059. https://doi.org/10.1016/J.ICARUS.2020.114059

Bertrand, T., Wilson, R. J., Kahre, M. A., Urata, R., & Kling, A. (2020). Simulation of the 2018 global dust storm on Mars using the nasa Ames Mars GCM: A multitracer approach. *Journal of Geophysical Research: Planets*, *125*(7), e2019JE006122. https://doi.org/10.1029/2019JE006122

Bibring, J.-P., Soufflot, A., Berthé, M., Langevin, Y., Gondet, B., Drossart, P., et al. (2004). OMEGA: Observatoire pour la Minéralogie, l'Eau, les Glaces et l'Activité. *ESASP*, *1240*, 37–49. https://ui.adsabs.harvard.edu/abs/2004ESASP1240.37B/abstract

Bonello, G., Bibring, J., Poulet, F., Gendrin, A., Gondet, B., Langevin, Y., & Fonti, S. (2003). Visible and infrared spectroscopy of minerals and mixtures with the OMEGA/MARS-EXPRESS instrument. *Planetary and Space Science*, *52*(1–3), 133–140. https://doi.org/10.1016/j.pss.2003.08.014

Cantor, B. A., James, P. B., Caplinger, M., & Wolff, M. J. (2001). Martian dust storms: 1999 Mars orbiter camera observations. *Journal of Geophysical Research*, *106*(E10), 23653–23687. https://doi.org/10.1029/2000JE001310

Conrath, B. J. (1975). Thermal structure of the Martian atmosphere during the dissipation of the dust storm of 1971. *Icarus*, *24*(1), 36–46. https://doi.org/10.1016/0019-1035(75)90156-6

Douté, S. (2013). Monitoring atmospheric dust spring activity at high southern latitudes on Mars using OMEGA. *Planetary and Space Science*, *96*, 1–21. https://doi.org/10.1016/j.pss.2013.12.017

Douté, S., Ceamanos, X., & Appéré, T. (2013). Retrieving atmospheric dust opacity on Mars by imaging spectroscopy at large angles. *Planetary and Space Science*, *85*, 38–52. https://doi.org/10.1016/J.PSS.2013.05.017

Forget, F., Hourdin, F., Fournier, R., Hourdin, C., Talagrand, O., Collins, M., et al. (1999). Improved general circulation models of the Martian atmosphere from the surface to above 80 km. *Journal of Geophysical Research*, *104*(E10), 24155–24175. https://doi.org/10.1029/1999JE001025

Forget, F., Spiga, A., Dolla, B., Vinatier, S., Melchiorri, R., Drossart, P., et al. (2007). Remote sensing of surface pressure on Mars with the Mars express/OMEGA spectrometer: 1. Retrieval method. *Journal of Geophysical Research*, *112*(E8), 8–15. https://doi.org/10.1029/2006JE002871

Gordon, I. E., Rothman, L. S., Hargreaves, R. J., Hashemi, R., Karlovets, E. V., Skinner, F. M., et al. (2022). The HITRAN2020 molecular spectroscopic database. *Journal of Quantitative Spectroscopy and Radiative Transfer*, *277*, 107949. https://doi.org/10.1016/J.JQSRT.2021.107949

Guha, B. K., Gebhardt, C., Young, R. M. B., Wolff, M. J., & Montabone, L. (2024). Seasonal and diurnal variations of dust storms in martian year 36 based on the EMM-EXI database. *Journal of Geophysical Research: Planets*, *129*(4), e2023JE008156. https://doi.org/10.1029/2023JE008156

Heavens, N. G., Kass, D. M., & Shirley, J. H. (2019a). Dusty deep convection in the Mars year 34 planet-encircling dust event. *Journal of Geophysical Research: Planets*, *124*(11), 2863–2892. https://doi.org/10.1029/2019JE006110

Heavens, N. G., Kass, D. M., Shirley, J. H., Piqueux, S., & Cantor, B. A. (2019b). An observational overview of dusty deep convection in martian dust storms. *Journal of the Atmospheric Sciences*, *76*(11), 3299–3326. https://doi.org/10.1175/JAS-D-19-0042.1

Heavens, N. G., McCleese, D. J., Richardson, M. I., Kass, D. M., Kleinböhl, A., & Schofield, J. T. (2011a). Structure and dynamics of the martian lower and middle atmosphere as observed by the Mars climate sounder: 2. Implications of the thermal structure and aerosol distributions for the mean meridional circulation. *Journal of Geophysical Research*, *116*(E1), E01010. https://doi.org/10.1029/2010JE003713

Heavens, N. G., Richardson, M. I., Kleinbhöl, A., Kass, D. M., McCleese, D. J., Abdou, W., et al. (2011b). The vertical distribution of dust in the Martian atmosphere during northern spring and summer: Observations by the Mars Climate Sounder and analysis of zonal average vertical dust profiles. *Journal of Geophysical Research*, *116*(E4), E04003. https://doi.org/10.1029/2010JE003691

Heavens, N. G., Richardson, M. I., Kleinböhl, A., Kass, D. M., McCleese, D. J., Abdou, W., et al. (2011c). Vertical distribution of dust in the Martian atmosphere during northern spring and summer: High-altitude tropical dust maximum at northern summer solstice. *Journal of Geophysical Research*, *116*(E1), E01007. https://doi.org/10.1029/2010JE003692

Hinson, D. P., & Wang, H. (2010). Further observations of regional dust storms and baroclinic eddies in the northern hemisphere of Mars. *Icarus*, *206*(1), 290–305. https://doi.org/10.1016/J.ICARUS.2009.08.019

Ignatiev, N. I., Grassi, D., & Zasova, L. V. (2005). Planetary Fourier spectrometer data analysis: Fast radiative transfer models. *Planetary and Space Science*, *53*(10), 1035–1042. https://doi.org/10.1016/J.PSS.2004.12.009

Ivanov, A. B., & Muhleman, D. O. (2001). Cloud reflection observations: Results from the Mars orbiter laser altimeter. *Icarus*, *154*(1), 190–206. https://doi.org/10.1006/ICAR.2001.6686

Jouglet, D., Poulet, F., Langevin, Y., Bibring, J. P., Gondet, B., Vincendon, M., & Berthe, M. (2009). OMEGA long wavelength channel: Data reduction during non-nominal stages. *Planetary and Space Science*, *57*(8–9), 1032–1042. https://doi.org/10.1016/J.PSS.2008.07.025

Jouglet, D., Poulet, F., Milliken, R. E., Mustard, J. F., Bibring, J. P., Langevin, Y., et al. (2007). Hydration state of the martian surface as seen by Mars express OMEGA: 1. Analysis of the 3 μm hydration feature. *Journal of Geophysical Research*, *112*(E8), 8–14. https://doi.org/10.1029/2006JE002846

Kahre, M. A., Murphy, J. R., & Haberle, R. M. (2006). Modeling the Martian dust cycle and surface dust reservoirs with the NASA Ames general circulation model. *Journal of Geophysical Research*, *111*(E6). https://doi.org/10.1029/2005JE002588

Kass, D. M., Kleinböhl, A., McCleese, D. J., Schofield, J. T., & Smith, M. D. (2016). Interannual similarity in the Martian atmosphere during the dust storm season. *Geophysical Research Letters*, *43*(12), 6111–6118. https://doi.org/10.1002/2016GL068978

Kazama, A. (2025). Kazama+2025, the data of figure1-13 [Dataset]. *Zenodo*. https://doi.org/10.5281/zenodo.14771625

Kuramoto, K., Kawakatsu, Y., Fujimoto, M., Araya, A., Barucci, M. A., Genda, H., et al. (2022). Martian moons exploration MMX: Sample return mission to phobos elucidating formation processes of habitable planets. *Earth, Planets and Space 2021*, *74*(1), 1–31. https://doi.org/10.1186/S40623-021-01545-7

Langevin, Y., Bibring, J. P., Montmessin, F., Forget, F., Vincendon, M., Douté, S., et al. (2007). Observations of the south seasonal cap of Mars during recession in 2004–2006 by the OMEGA visible/near-infrared imaging spectrometer on board Mars Express. *Journal of Geophysical Research*, *112*(E8), E08S12. https://doi.org/10.1029/2006JE002841

Lemmon, M. T., Wolff, M. J., Smith, M. D., Clancy, R. T., Banfield, D., Landis, G. A., et al. (2004). Atmospheric imaging results from the Mars exploration Rovers: Spirit and opportunity. *Science*, *306*(5702), 1753–1756. https://doi.org/10.1126/SCIENCE.1104474

Leseigneur, Y., & Vincendon, M. (2023). OMEGA/Mars express: A new Martian atmospheric dust hunter. *Icarus*, *392*, 115366. https://doi.org/10.1016/J.ICARUS.2022.115366

Liuzzi, G., Villanueva, G. L., Crismani, M. M. J., Smith, M. D., Mumma, M. J., Daerden, F., et al. (2020). Strong variability of martian water ice clouds during dust storms revealed from ExoMars trace gas orbiter/NOMAD. *Journal of Geophysical Research: Planets*, *125*(4), e2019JE006250. https://doi.org/10.1029/2019JE006250

Määttänen, A., Fouchet, T., Forni, O., Forget, F., Savijärvi, H., Gondet, B., et al. (2009). A study of the properties of a local dust storm with Mars Express OMEGA and PFS data. *Icarus*, *201*(2), 504–516. https://doi.org/10.1016/J.ICARUS.2009.01.024

Madeleine, J. B., Forget, F., Spiga, A., Wolff, M. J., Montmessin, F., Vincendon, M., et al. (2012). Aphelion water-ice cloud mapping and property retrieval using the OMEGA imaging spectrometer onboard Mars Express. *Journal of Geophysical Research*, *117*(E11), E00J07. https://doi.org/10.1029/2011JE003940

Martin, L. J., & Zurek, R. W. (1993). An analysis of the history of dust activity on Mars. *Journal of Geophysical Research*, *98*(E2), 3221–3246. https://doi.org/10.1029/92JE02937

Millour, E., Forget, F., Spiga, A., Pierron, T., Bierjon, A., Montabone, L., et al. (2022). The Mars Climate database. *Europlanet Science Congress 2022*, EPSC2022-786. https://doi.org/10.5194/epsc2022-786

Montabone, L., Forget, F., Millour, E., Wilson, R. J., Lewis, S. R., Cantor, B., et al. (2015). Eight-year climatology of dust optical depth on Mars. *Icarus*, *251*, 65–95. https://doi.org/10.1016/J.ICARUS.2014.12.034

Mulholland, D. P., Read, P. L., & Lewis, S. R. (2013). Simulating the interannual variability of major dust storms on Mars using variable lifting thresholds. *Icarus*, *223*(1), 344–358. https://doi.org/10.1016/J.ICARUS.2012.12.003

Newman, C. E., Lewis, S. R., Read, P. L., & Forget, F. (2002). Modeling the Martian dust cycle 2. Multiannual radiatively active dust transport simulations. *Journal of Geophysical Research*, *107*(E12), 7-1–7-15. https://doi.org/10.1029/2002JE001920

Ockert-Bell, M. E., Bell, J. F., Pollack, J. B., McKay, C. P., & Forget, F. (1997). Absorption and scattering properties of the Martian dust in the solar wavelengths. *Journal of Geophysical Research*, *102*(E4), 9039–9050. https://doi.org/10.1029/96JE03991

Ogohara, K., Nakagawa, H., Aoki, S., Kouyama, T., Usui, T., Terada, N., et al. (2022). The Mars system revealed by the Martian Moons eXploration mission. *Earth, Planets and Space 2021*, *74*(1), 1–32. https://doi.org/10.1186/S40623-021-01417-0

PSA. (2023). Mex-m-omega-2-edr-flight [Dataset]. *European Space Agency*. https://doi.org/10.57780/ESA-AM1BWAQ

Sánchez-Lavega, A., del Río-Gaztelurrutia, T., Spiga, A., Hernández-Bernal, J., Larsen, E., Tirsch, D., et al. (2024). Dynamical phenomena in the martian atmosphere through Mars Express imaging. *Space Science Reviews*, *220*(1), 1–25. https://doi.org/10.1007/S11214-024-01047-4/FIGURES/11

Smith, D. E., Zuber, M. T., Frey, H. V., Garvin, J. B., Head, J. W., Muhleman, D. O., et al. (2001). Mars orbiter Laser altimeter: Experiment summary after the first year of global mapping of Mars. *Journal of Geophysical Research*, *106*(E10), 23689–23722. https://doi.org/10.1029/2000JE001364

Smith, M. D., Badri, K., Atwood, S. A., Edwards, C. S., Christensen, P. R., Wolff, M. J., et al. (2022). EMIRS observations of the aphelion-season Mars atmosphere. *Geophysical Research Letters*, *49*(15), e2022GL099636. https://doi.org/10.1029/2022GL099636

Smith, M. D., Martínez, G. M., Sebastián, E., Lemmon, M. T., Wolff, M. J., Apéstigue, V., et al. (2023). Diurnal and seasonal variations of aerosol optical depth observed by MEDA/TIRS at Jezero Crater, Mars. *Journal of Geophysical Research: Planets*, *128*(1), e2022JE007560. https://doi.org/10.1029/2022JE007560

Smith, M. D., & Smith, D. M. (2004). Interannual variability in TES atmospheric observations of Mars during 1999-2003. *Icarus*, *167*(1), 148–165. https://doi.org/10.1016/J.ICARUS.2003.09.010

Spiga, A., Faure, J., Madeleine, J. B., Määttänen, A., & Forget, F. (2013). Rocket dust storms and detached dust layers in the Martian atmosphere. *Journal of Geophysical Research: Planets*, *118*(4), 746–767. https://doi.org/10.1002/JGRE.20046

Stamnes, K., Tsay, S.-C., Wiscombe, W., & Jayaweera, K. (1988). Numerically stable algorithm for discrete-ordinate-method radiative transfer in multiple scattering and emitting layered media. *Applied Optics*, *27*(12), 2502. https://doi.org/10.1364/AO.27.002502

Titov, D. V., Fedorova, A. A., & Haus, R. (2000). A new method of remote sounding of the Martian aerosols by means of spectroscopy in the 2.7 μm CO2 band. *Planetary and Space Science*, *48*(1), 67–74. https://doi.org/10.1016/S0032-0633(99)00077-X
Toigo, A. D., Lee, C., Newman, C. E., & Richardson, M. I. (2012). The impact of resolution on the dynamics of the martian global atmosphere: Varying resolution studies with the MarsWRF GCM. *Icarus*, *221*(1), 276–288. https://doi.org/10.1016/J.ICARUS.2012.07.020
Toigo, A. D., Smith, M. D., Seelos, F. P., & Murchie, S. L. (2013). High spatial and temporal resolution sampling of Martian gas abundances from CRISM spectra. *Journal of Geophysical Research: Planets*, *118*(1), 89–104. https://doi.org/10.1029/2012JE004147
Vincendon, M., Audouard, J., Altieri, F., & Ody, A. (2015). Mars Express measurements of surface albedo changes over 2004–2010. *Icarus*, *251*, 145–163. https://doi.org/10.1016/j.icarus.2014.10.029
Vincendon, M., Langevin, Y., Poulet, F., Bibring, J. P., & Gondet, B. (2007). Recovery of surface reflectance spectra and evaluation of the optical depth of aerosols in the near-IR using a Monte Carlo approach: Application to the OMEGA observations of high-latitude regions of Mars. *Journal of Geophysical Research*, *112*(E8), 8–13. https://doi.org/10.1029/2006JE002845
Vincendon, M., Langevin, Y., Poulet, F., Bibring, J. P., Gondet, B., & Jouglet, D. (2008). Dust aerosols above the south polar cap of Mars as seen by OMEGA. *Icarus*, *196*(2), 488–505. https://doi.org/10.1016/J.ICARUS.2007.11.034
Vincendon, M., Langevin, Y., Poulet, F., Pommerol, A., Wolff, M., Bibring, J. P., et al. (2009). Yearly and seasonal variations of low albedo surfaces on Mars in the OMEGA/MEx dataset: Constraints on aerosols properties and dust deposits. *Icarus*, *200*(2), 395–405. https://doi.org/10.1016/J.ICARUS.2008.12.012
Wang, C., Forget, F., Bertrand, T., Spiga, A., Millour, E., & Navarro, T. (2018). Parameterization of rocket dust storms on Mars in the LMD martian GCM: Modeling details and validation. *Journal of Geophysical Research: Planets*, *123*(4), 982–1000. https://doi.org/10.1002/2017JE005255
Wang, H., & Richardson, M. I. (2015). The origin, evolution, and trajectory of large dust storms on Mars during Mars years 24–30 (1999–2011). *Icarus*, *251*, 112–127. https://doi.org/10.1016/J.ICARUS.2013.10.033
Wolff, M. J., & Clancy, R. T. (2003). Constraints on the size of martian aerosols from thermal emission spectrometer observations. *Journal of Geophysical Research*, *108*(E9), 5097. https://doi.org/10.1029/2003JE002057
Wolff, M. J., Smith, M. D., Clancy, R. T., Arvidson, R., Kahre, M., SeelosIV., F., et al. (2009). Wavelength dependence of dust aerosol single scattering albedo as observed by the Compact Reconnaissance Imaging Spectrometer. *Journal of Geophysical Research*, *114*(E2), E00D04. https://doi.org/10.1029/2009JE003350
Wolff, M. J., Vincendon, M., Smith, M. D., Clancy, R. T., Langevin, Y., Arvidson, R. E., et al. (2019). *An updated dust aerosol model for Mars* (pp. P41B–3407). AGUFM. Retrieved from https://ui.adsabs.harvard.edu/abs/2019AGUFM.P41B3407W/abstract